Lithofacies and Diagenetic Controls on Tight Silty and Sandy Upper Triassic Reservoirs of the Heshui Oil Field (Ordos Basin, North China)

Chenlin Hu[1,2], Changcheng Han[1,2]*, Jijun Tian[1,2]*, Zhiqiang Fu[1,2], Jinghui Ma[1,2], and Thomas J. Algeo[3,4,5]

[1]School of Geology and Mining Engineering, Xinjiang University
[2]Xinjiang Key Laboratory of Geodynamic Processes and Metallogenic Prognosis of the Central Asian Orogenic Belt, Xinjiang University
[3]Department of Geology, University of Cincinnati
[4]State Key Laboratory of Geological Processes and Mineral Resources, China University of Geosciences, Wuhan
[5]State Key Laboratory of Biogeology and Environmental Geology, China University of Geosciences, Wuhan

Summary

Tight oil, present in reservoirs of low porosity and permeability, can be regarded as a kind of unconventional resource. The tightening process in this kind of reservoir is controlled by the lithology and diagenetic history of the host formation. Upper Triassic Yanchang Formation siltstones and sandstones are the main reservoirs for hydrocarbon accumulation in the Heshui Oil Field (HOF), southwestern Ordos Basin. The reservoirs exhibit low porosity, low permeability, and strong heterogeneity. In recent years, numerous drillcores have been recovered from these units, but the porosity-permeability characteristics and burial history of these silty and sandy reservoirs have not yet been reported in detail. In this study, an integrated analysis of the lithofacies, diagenesis, and reservoir characteristics of the siltstones and sandstones was achieved using a combination of core and thin section, grain size, scanning electron microscopy (SEM), X-ray diffraction (XRD), $\delta^{13}C$ and $\delta^{18}O$, mercury intrusion capillary pressure (MICP), and porosity and permeability data. Our primary goals were to quantify the porosity-permeability characteristics of these silty and sandy reservoirs, restore their diagenetic histories, and examine the paragenetic relationship of reservoir tightness to hydrocarbon accumulation. The silty and sandy reservoirs represent braided river delta facies consisting of compositionally and texturally immature sediments. In the burial environment, they underwent complex diagenetic processes that reduced porosity from an initial average of ~38% to the present ~8%. Porosity-destructive processes included compaction (~ –12.5%) and cementation (~ –21%), with increases in porosity related to grain dissolution (~ +2.2%) and tectonic fractures (~ +1.1%). The reservoirs underwent four diagenetic stages: (1) Penesyngenetic and Eogenetic A Stage (Late Triassic-Early Jurassic); (2) Eogenetic B Stage (Late Jurassic); (3) Early Mesogenetic A Stage (Early Cretaceous); and (4) Late Mesogenetic A Stage (Late Cretaceous to recent). Hydrocarbon charging of these reservoirs occurred in three pulses. Existing pore space was partly filled by hydrocarbons during the Eogenetic B Stage. A second hydrocarbon charging event occurred during the Early Mesogenetic A Stage, when residual primary intergranular pores and secondary dissolution pores were filled. A third hydrocarbon charging event occurred during the Late Mesogenetic A Stage, when the reservoirs were tight. Siltstone beds deposited in delta front environments are the main future exploration targets in the Chang 6 to 8 members. The results of this study provide a useful reference framework for future exploration of hydrocarbon resources in the Upper Triassic Yanchang Formation of the HOF, as well as potential insights into the evolution of similarly tight reservoirs in other basins.

Introduction

In the field of oil and gas exploration, conventional resources are declining in importance, and unconventional resources are playing an increasingly important strategic role (Suboyin et al. 2020; Syed et al. 2021). Tight oil, as a kind of unconventional resource, refers to oil accumulations in tight reservoirs within which long-distance migration is impossible (Syah et al. 2021). There are two main types of tight oil occurrences: (1) reservoir intercalations within source rocks, such as the Bakken Shale (Donohue and Barrie 2021), Niobrara Shale (Uzun and Kazemi 2021), Barnett Shale (Sanguinito et al. 2020), and Eagle Ford Shale (Amosu et al. 2021); and (2) reservoir layers adjacent to source rocks, including tight sandstones [e.g., Upper Cretaceous of the Piceance Basin, Colorado, USA (Fall et al. 2015); Upper Carboniferous of the Saxony Basin, Northwest Germany (Busch et al. 2019); and Oligocene of the onshore Central Sarawak, Borneo (Adepehin et al. 2020)]; and tight carbonates [e.g., Turonian-Campanian Kometan Formation of northern Iraq (Rashid et al. 2015); Eocene of the October Oil Field, Gulf of Suez rift basin, Egypt (Radwan et al. 2021)]. These reservoirs are characterized by low porosity and low permeability, and they tend to have more complex reservoir formation mechanisms, finer pore throats, higher interstitial contents, and more difficult exploitation histories than conventional reservoirs (Fraser and Pedersen 2021).

Reservoir sandstones characterized by porosity less than 10% and permeability less than 0.1 md are referred to as tight sandstones (Zou et al. 2012). The last few decades have yielded significant research devoted to these tight sandstone reservoirs, primarily because of their known propensity for serving as hydrocarbon carrier beds (Orlov et al. 2021). The porosity-permeability characteristics of tight sandy reservoirs are controlled by their lithofacies and diagenetic histories (Mehrabi et al. 2021). Depositional facies influence the texture, mineral composition, and pore configuration of a sedimentary deposit (Sadeghi et al. 2021), and these features are subsequently modified by diagenesis (Abrajevitch 2020), together influencing reservoir quality (Kassem et al. 2021). Reservoir quality is degraded by destructive

*Corresponding author; email: hanchangcheng@xju.edu.cn; tianxju@yahoo.com

Original SPE manuscript received for review 19 September 2022. Revised manuscript received for review 25 October 2022. Paper (SPE 214289) peer approved 28 November 2022. Supplementary materials are available in support of this paper and have been published online under Supplementary Data at https://doi.org/10.2118/214289-PA. SPE is not responsible for the content or functionality of supplementary materials supplied by the authors.

diagenetic processes such as compaction and cementation, whereas it can be enhanced by constructive diagenetic processes such as grain dissolution and tectonic fracturing (Ettinger et al. 2021).

The Ordos Basin in northern China is a major area of oil and gas resources (Zou et al. 2019; Hu et al. 2020a). The siltstone and sandstone reservoirs of the Upper Triassic Yanchang Formation are the main exploration targets, especially in the HOF (Ji et al. 2009; Zheng et al. 2019). The reservoirs are largely developed in braided river delta facies (Lin et al. 2008; Wang 2016) and underwent complex diagenetic processes (Ma 2017; Gao et al. 2019) that significantly reduced porosity and permeability (now ~8.1% and ~0.08 md, respectively) and generated substantial reservoir heterogeneity (Gao et al. 2019; Zheng et al. 2019). Hydrocarbon exploration and development of these units have been limited by a poor understanding of their oil-forming and trapping mechanisms (Ran et al. 2016; Cao et al. 2019), a gap that is addressed by the present study.

The diagenetic processes and history of the Yanchang Formation in the HOF are complex (Ren et al. 2019; Gu et al. 2021). Previous studies have investigated the diagenetic history of this unit, including compaction, cementation, and dissolution (Lai et al. 2020; Gu et al. 2021) but did not address the issue of tectonic fracturing (Scientific Question I). Tectonic fracturing is a constructive diagenetic process that has the potential to improve tight reservoir quality. Additionally, the dynamics and interrelationship of compaction and cementation are major diagenetic modification mechanisms in tight siltstones and sandstones (Dou et al. 2018; Shi et al. 2021). However, published works have not considered in detail how these factors affected reservoir quality in the Yanchang Formation (Scientific Question II). Furthermore, basin geotectonic and burial histories play a major role in determining the depth of occurrence of tight siltstones and sandstones (Wang et al. 2017; Ren et al. 2019). Because there is no clear understanding of the reservoir evolution of the Yanchang Formation (Scientific Question III), earlier studies have arrived at differing conclusions regarding the relationship between hydrocarbon charging and reservoir development, with oil accumulation inferred to have been before (Deng et al. 2009), concurrent with (Tian et al. 2011), or after porosity reduction (Wang et al. 2017). These uncertainties encumber exploration for tight oil in the Yanchang Formation. To address the three scientific problems above, it is necessary to better understand the timing and mechanisms of porosity development in the tight siltstones and sandstones of the Upper Triassic Yanchang Formation. Insights gained from this study will facilitate prediction of reservoir distribution in the HOF.

In the present study, an integrated analysis of lithofacies, diagenesis, and reservoir characteristics of the siltstones and sandstones within the Chang 6 to 8 members of the Yanchang Formation in the HOF was undertaken based on core and thin-section observations, grain-size analysis, SEM, XRD, $\delta^{13}C$ and $\delta^{18}O$ measurements, MICP analysis, and porosity and permeability testing. The aims of this study were to quantify the porosity-permeability characteristics of these silty and sandy reservoirs, determine their diagenetic histories, and examine the paragenetic relationship of reservoir tightness to hydrocarbon accumulation. The results of this study provide a useful reference framework for future exploration of hydrocarbon resources in the Upper Triassic Yanchang Formation of the HOF as well as potential insights into the evolution of similarly tight reservoirs in other basins.

Geological Setting

The Ordos Basin, with an area of ~2.5×10^5 km^2, is located in North China, covering parts of Gansu, Ningxia, Shanxi, Inner Mongolia, and Shaanxi provinces (**Fig. 1a;** Yang et al. 2005; Hu et al. 2020b). It is an intracratonic basin developed on Archean granulite and Lower Proterozoic greenschist of the North China Craton (Chang et al. 2019). The basin is divided into six structural units—the Yimeng Uplift to the north, the Weibei Uplift to the south, the Western Edge Overthrust Belt and the Tianhuan Depression to the west, the Jinxi Flexure Belt to the east, and the Yishan Ramp in the central part of the basin (Yang et al. 2005; Jiang et al. 2012). This study focuses on the HOF, with an area of ~1.0×10^3 km^2, located on the southwestern Yishan Ramp (**Figs. 1b and 1c**; Yan et al. 2020).

The North China Craton shifted slowly northward across the Paleo-Northern Hemisphere during the Triassic Period, based on mean Paleo latitudes of 18.3°N, 21.4°N, and 25.4°N for the Early, Middle, and Late Triassic, respectively (Ji et al. 2008). The climate of this craton was hot, reflecting its low-latitude location. Climate conditions slowly became more humid, progressing from semi-arid and strongly oxidizing during the Early Triassic to semi-humid and weakly oxidizing during the Middle Triassic and to humid and relatively reducing during the Late Triassic, reflecting a shift out of the arid subtropical belt into the wetter temperate zone with time (Li et al. 2020).

The Ordos Basin accumulated marine facies before the Permian (Hu et al. 2020a; Zhao et al. 2020), followed by a shift to transitional marine-continental facies in the Early Permian and then to purely continental facies in the Middle to Late Triassic (Yang et al. 2019). Despite the absence of Silurian to Lower Carboniferous strata as well as Upper Cretaceous strata, Paleozoic to Cenozoic formations are distributed throughout the basin (Wang et al. 2017). The Mesozoic continental facies contain significant oil reserves in siltstone and sandstone reservoirs, especially in the Upper Triassic Yanchang Formation, which has a total thickness of 1000 to 1330 m (**Fig. 2;** Guo et al. 2018). The Yanchang Formation is subdivided into the Chang 1 to 10 members (from top to bottom), recording the development, evolution, and termination of a large lacustrine basin (He et al. 2019). The Chang 10 to 7 members comprise transgressive deposits from the early stage of lake development, while the Chang 6 to 1 members comprise highstand to regressive deposits of the latter stages of lake development (Guo et al. 2014; Zou et al. 2019).

This study focuses on the Chang 6 to 8 members of the Yanchang Formation. The Chang 6 Member, deposited as braided river and delta front facies, is a mixture of sandstone, siltstone, and shale with aggregate thicknesses of 45±5, 35±15, and 15±5 m, respectively. The Chang 7 Member, deposited as prodelta to deep-lake facies, is a mixture of sandstone, siltstone, and shale with aggregate thicknesses of 5±2, 25±5, and 70±10 m, respectively. The Chang 8 Member, deposited as braided river and delta front facies, is a mixture of sandstone and siltstone with aggregate thicknesses of 45±15 and 30±5 m, respectively (**Fig. 2**; Guo et al. 2014; Zou et al. 2019).

Sampling and Methods

A total of 72 drillcores from the HOF representing more than 1700 m of stratigraphic section were examined in this study (Table S-1 of the Supplemental Material)**.** Copious descriptions, measurements, and photos were made for each drillcore, from which nine (ZT-16, ZT-22, ZT-24, ZT-28, ZT-57, ZT-81, NT-87, NT-93, and NT-96) were selected for sample collection and analysis, including thin sections, grain-size determinations, SEM, XRD, $\delta^{13}C$ and $\delta^{18}O$ measurements, MICP, and porosity and permeability testing **(Fig. 1c)**.

Thin-Section Analysis. A total of 1,053 samples were prepared as thin sections and examined using a standard petrographic microscope (model: Carl Zeiss Axio Scope A1). These samples were impregnated with blue resin to highlight porosity and stained with Alizarin Red S and K-ferricyanide for mineral determination. Mineral identification procedures followed the China National Identification for Thin Section of Rocks Standard of SY/T 5368-2000. Thin-section porosity and mineralogical proportions were calculated by point counting using a 20×30 grid (n = 600 observations per sample).

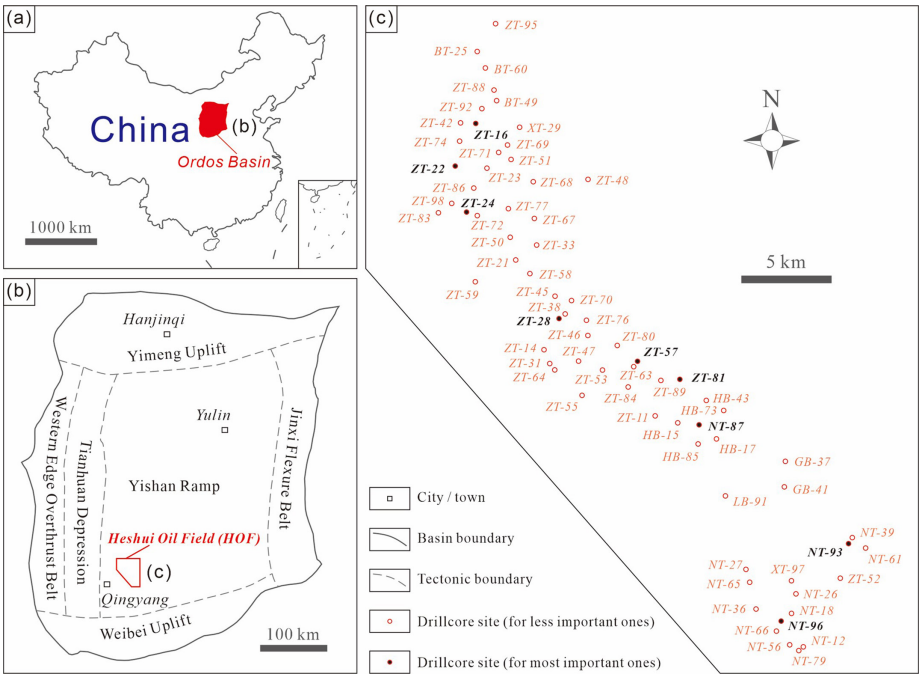

Fig. 1—Regional index map showing the study area. (a) Simplified map of China showing the Ordos Basin (after Yang et al. 2005). (b) Structural divisions of the Ordos Basin showing the HOF (after Jiang et al. 2012). (c) Simplified map of the HOF showing drillcore locations (detailed information is given in Table S-1 of the Supplemental Material).

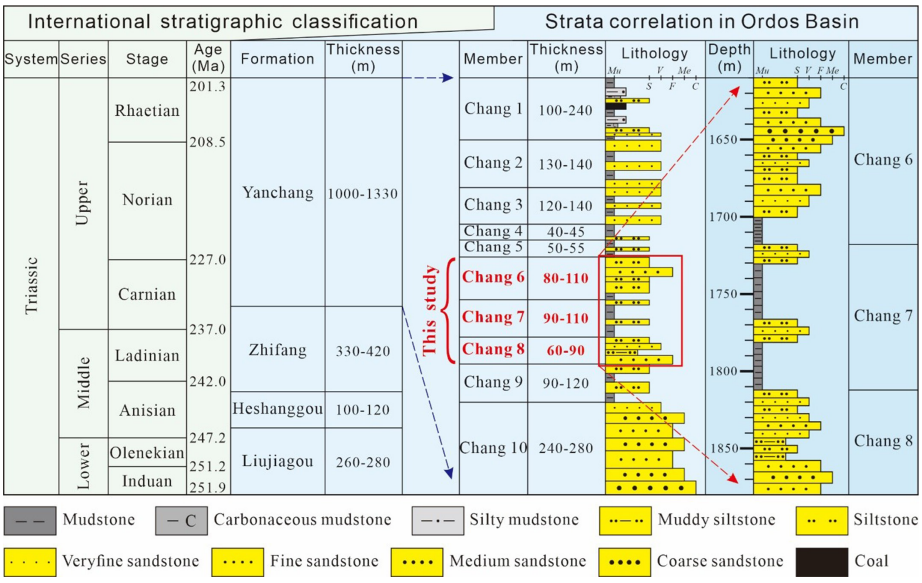

Fig. 2—Triassic stratigraphy in the Ordos Basin (after Guo et al. 2014; Zou et al. 2019). Geochronology from Cohen et al. (2013) and Guo et al. (2014). Grain-size classification: *Mu* = mudstone (<0.0039 mm); *S* = siltstone (0.0039–0.0625 mm); *V* = very fine-grained sandstone (0.0625–0.125 mm); *F* = fine-grained sandstone (0.125–0.25 mm); *Me* = medium-grained sandstone (0.25–0.5 mm); *C* = coarse-grained sandstone (0.5–1 mm).

Grain-Size Determinations. Grain-size experiments were performed on 808 samples. Before analysis, the samples were disaggregated by breaking them into small pieces using a mortar and pestle and then dissolving the binding material between individual grains. Each sample was subjected to pyrolysis at 400°C for no less than 4 hours. Organic matter was removed by adding an excess 6% hydrogen peroxide solution, after which the sample was moved to an electric water bath where it was stirred and boiled until the reaction was complete and all evolved carbon dioxide and any remaining oxygen were released. The samples were then placed in an oven at a constant temperature of 105°C. After natural cooling, the samples were taken out and tested using a laser particle size analysis instrument (model: Mastersize-2000). Operational procedures followed the China National Analysis Method for Particle Size of Clastic Rocks Standard of SY/T 5434-2018.

SEM. A total of 291 freshly broken rock fragments coated with a thin layer of gold were examined using a JEOLJSM-T330 scanning electron microscope equipped with a back-scattered electron detector. SEM analyses of bulk rock were conducted at 15 to 20 kV acceleration voltage with beam current of 0.6 nA. Samples were observed at magnifications ranging from 200× to 2000X. SEM was used to confirm clay mineral identifications as well as to determine pore structure, types of cement, and modes of clay occurrence within the pore spaces of the study samples.

XRD. A total of 260 samples were examined for whole-rock (bulk) together with clay fraction (less than 2 μm) mineralogy using XRD. Each sample (~5 g) was crushed and milled in ethanol using a McCrone micronizing mill and then dried in an oven at 60°C. Next, randomly oriented powders were top-loaded into polymethylmethacrylate containers with shallow circular sample pits. The powder diffraction patterns were then generated using a D/MAX 2500 X-ray diffractometer with Cu Kα radiation. The generated XRD traces were studied for mineral phase identification using the search-match module of the evaluation software in conjunction with reference databases of the International Center for Diffraction Data Powder Diffraction File 2 as well as Crystallography Open Database. Mineral phases were determined from the Rietveld quantitative XRD refinement method (Xi et al. 2019).

$\delta^{13}C$ and $\delta^{18}O$ Measurements. A total of 54 paired $\delta^{13}C$ and $\delta^{18}O$ measurements were performed. Each sample was ground to powder with a grain size of less than 90 μm and baked at 110°C for 2 hours. For each isotopic analysis, a total of 20 mg of sample powder was placed in a reaction bottle, and 5 mL orthophosphoric acid with 99% concentration was added. After evacuation of air from the reaction vessel, the sample and the orthophosphoric acid were mixed to react with each other at a temperature of 75°C for 16 hours. A liquid nitrogen cold well (−80 to −70°C) was then used to collect the carbon dioxide. After purification, the carbon dioxide was delivered to a thermal mass spectrometer (model: MAT-252) for analysis. The standard sample GBW04405 was used for monitoring analytical accuracy. Results are reported in per mille units relative to the V-PDB scale.

MICP. A total of 25 representative samples were examined using a mercury porosimeter (Pore Sizer 9320) for MICP study, following the China National Rock Capillary Pressure Measurement Standard of GB/T 29171-2012. Using the logarithm of capillary pressure as ordinate and cumulative mercury saturation as abscess, the relationship curve between capillary pressure and mercury saturation was drawn on a semilogarithmic coordinate graph. Saturation is 0 to 100% from right to left. Maximum mercury injection saturation ($S_{HG\max}$) is the mercury saturation corresponding to the peak pressure on the mercury injection curve. Minimum residual mercury saturation ($S_{HG\min}$) is the mercury saturation corresponding to the minimum pressure on the mercury ejection curve. Displacement pressure (D_p) is the capillary pressure at which mercury starts continuously to enter the maximum throat of the rock sample. Mercury ejection efficiency (W_e) is the percentage of the volume of mercury removed from the sample to the total volume of mercury injected before depressurization.

Porosity and Permeability Testing. A total of 502 samples were examined for porosity and permeability. The permeability measurements were performed on cut plugs (25 mm in diameter and 50 mm in height) using a permeameter (ULTRAPERMTM-200). Sample plugs were dried in a vacuum at 120°C for 24 to 48 hours. Then, they were put in the permeameter as well as injected with nitrogen at confining pressures of 0.69 and 2.76 MPa. Next, the same samples were used in porosity determinations using a porosimeter (ULTRAPORE-200A). The grain volume of each sample was calculated on the basis of Boyle's law derived from the corresponding pressure as well as volume, from which the porosity of the grain as well as measured bulk volume was calculated [i.e., porosity = (bulk volume – grain volume) / bulk volume].

Results

The lithofacies and reservoir analysis of the study units were based on observations of lithology, bedding, sedimentary textures, and grain types in cores, thin sections, and SEM as well as mercury injection, grain-size analysis, XRD, $\delta^{13}C$ and $\delta^{18}O$ measurements, and porosity and permeability testing. Samples were evaluated using standard descriptive and interpretative criteria. A total of five lithofacies types were recognized in the study units: siltstones (0.0039−0.0625 mm), very fine-grained sandstones (0.0625−0.125 mm), fine-grained sandstones (0.125−0.25 mm), medium-grained sandstones (0.25−0.5 mm), and coarse-grained sandstones (0.5−1 mm).

Reservoir Characteristics. ***Pore and Pore-Throat Types.*** The siltstones and sandstones of the Chang 6 to 8 members contain both primary and secondary porosity. The former pores usually have triangular or irregular shapes and strong oil staining that often appears at residual intergranular pores **(Fig. 3).** Moreover, the latter pores are basically generated by the dissolution of feldspar crystals as well as rock fragments **(Figs. 3a, 4a, and 5a)**. In addition, intercrystalline pores and microfractures can occur **(Fig. 5 and Fig. S-1a).** Pore throats are small, look like pipe and sheet, and have an uneven size distribution **(Figs. 5 and 6).** The mercury saturation parameters of the study samples show variation as a function of grain size (**Table 1** and Table S-2 in the Supplemental Material). The siltstones, very fine-grained sandstones, fine-grained sandstones, medium-grained sandstones, and coarse-grained sandstones yield saturation profiles corresponding to peak pressures on the mercury injection curve of 80.4, 82.2, 78.4, 83.2, and 79.3, respectively; minimum pressures on the mercury ejection curve of 64.3, 61.9, 51.9, 59.4, and 54.7%, respectively; a mercury ejection efficiency of 20.2, 24.8, 32.6, 28.3, and 31.3%, respectively; a displacement pressure of 0.18, 0.30, 0.64, 1.12, and 1.68 MPa, respectively; and pore-throat radii of 3.81, 1.88, 0.85, 0.52, and 0.39 μm, respectively **(Fig. 7).**

Porosity and Permeability. The siltstones and sandstones of the Chang 6 to 8 members have low porosity and low permeability. The porosity and permeability of the study samples show variation as a function of grain size **(Table 2).** For siltstones, porosity ranges from 4.0 to 11.5%, with a mean of 8.9%, horizontal permeability ranges from 0.026 to 0.938 md, with a mean of 0.144 md, and a porosity-permeability correlation of $R^2 = 0.17$ **(Figs. 8a, 8b, and 8c).** For very fine-grained sandstones, porosity ranges from 3.5 to 11.2%, with a mean of 8.3%, horizontal permeability ranges from 0.018 to 0.190 md, with a mean of 0.081 md, and a porosity-permeability correlation of $R^2 = 0.56$ **(Figs. 8d, 8e, and 8f)**. For fine-grained sandstones, porosity ranges from 1.7 to 10.7%, with a mean of 8.1%, horizontal permeability ranges from 0.014 to 0.142 md, with a mean of 0.062 md, and a porosity-permeability correlation of $R^2 = 0.45$ **(Figs. 8g, 8h, and 8i)**. For medium-grained sandstones, porosity ranges from 2.0 to 10.2%, with a mean of 7.7%, horizontal permeability ranges from 0.004 to 0.103 md, with a mean of 0.048 md, and a porosity-permeability correlation of $R^2 = 0.34$ **(Figs. 8j, 8k, and 8l)**. For coarse-grained sandstones, porosity ranges from 2.9 to 9.7%, with a mean of 7.5%, horizontal permeability ranges from 0.004 to 0.078 md, with a mean of 0.043 md, and a porosity-permeability correlation of $R^2 = 0.34$ **(Figs. 8m, 8n, and 8o)**.

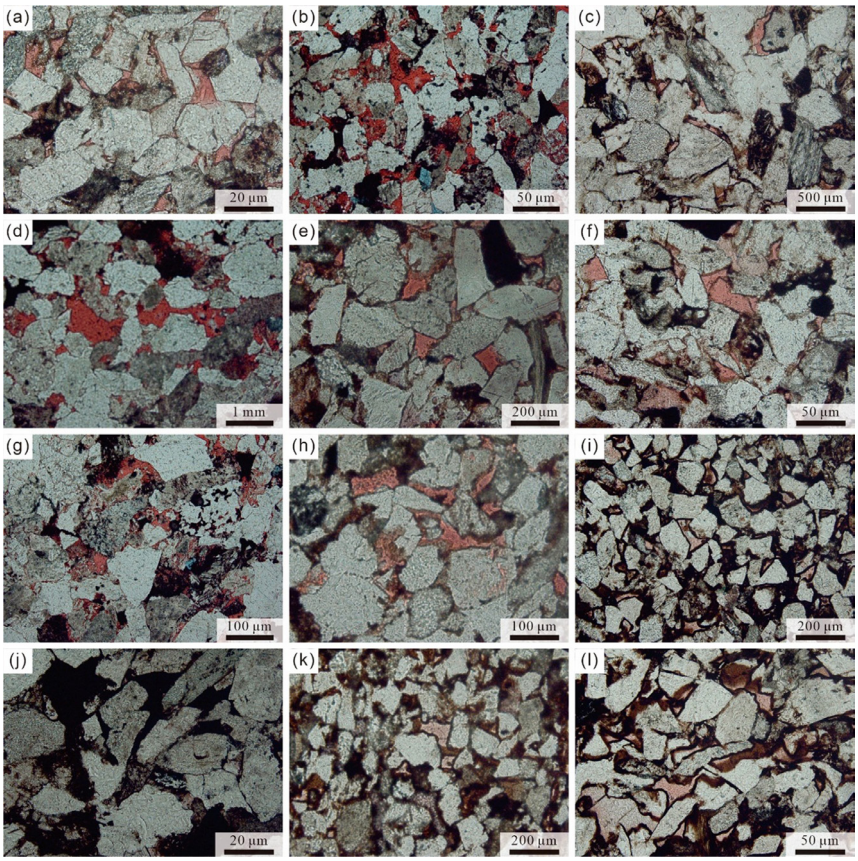

Fig. 3—Selected thin-section photographs (plain-polarized light) showing the microscopic features of siltstones and sandstones with a large amount of oil staining in Chang 6 to 8 members of the Yanchang Formation. (a) Siltstone with intergranular and dissolution pores containing calcite cement and oil staining, Drillcore ZT-28 at 1821.6 m (Chang 8 Member). (b) Very fine-grained sandstone with intergranular and dissolution pores containing calcite cements and oil staining, Drillcore ZT-28 at 1385.6 m (Chang 6 Member). (c) Medium-grained sandstone with intergranular and dissolution pores containing calcite cements and oil staining, Drillcore ZT-28 at 1825.4 m (Chang 8 Member). (d) Coarse-grained sandstone with intergranular and dissolution pores containing calcite cement and oil staining, Drillcore ZT-28 at 1387.5 m (Chang 6 Member). (e) Medium-grained sandstone with intergranular and dissolution pores containing calcite cements and oil staining, cracks developed on the surface of quartz grains, Drillcore ZT-28 at 1818.9 m (Chang 8 Member). (f) Siltstone with intergranular and dissolution pores containing calcite cements and oil staining, Drillcore ZT-28 at 1851.5 m (Chang 8 Member). (g) Very fine-grained sandstone with intergranular and dissolution pores containing calcite cement and oil staining, Drillcore ZT-28 at 1384.3 m (Chang 6 Member). (h) Very fine-grained sandstone with intergranular and dissolution pores containing calcite cements and oil staining, Drillcore ZT-28 at 1823.3 m (Chang 8 Member). (i) Fine-grained sandstone showing intergranular and dissolution pores with heavy oil staining, Drillcore ZT-28 at 1883.0 m (Chang 8 Member). (j) Siltstone showing intergranular pores with heavy oil staining, Drillcore ZT-28 at 1829.3 m (Chang 8 Member). (k) Fine-grained sandstone with intergranular and dissolution pores containing calcite cements and oil staining, particles are coated by chlorite cutan, Drillcore ZT-28 at 1881.4 m (Chang 8 Member). (l) Siltstone with intergranular pores, chlorite coating, and oil staining, Drillcore ZT-28 at 1886.1 m (Chang 8 Member).

The present porosities of the study samples are a product of their complex diagenetic histories. We calculated the initial porosity of each sample to investigate its porosity history and to quantitatively characterize the tightness of each reservoir layer. Although the initial porosity cannot be measured directly, it can be estimated using the parameters of primary components. Beard and Weyl (1973) studied the initial porosity of natural grains by artificial mixtures experimentally and demonstrated that different sorting coefficients have very different porosities. Accordingly, Scherer (1987) established the following expression to calculate the initial porosity (φ_o) in units of percent (%):

$$\varphi_0 = 20.91 + 22.90 / S, \quad (1)$$

where S represents the Trask sorting coefficient.

The S value of siltstones, very fine-grained sandstones, fine-grained sandstones, medium-grained sandstones, and coarse-grained sandstones were set to 1.26±0.5, 1.31±0.7, 1.37±0.6, 1.42±0.6, and 1.46±0.9, respectively. Consequently, the calculated initial porosities of the above five lithofacies are 39.1±0.7%, 38.4±1.0%, 37.6±0.8%, 37.0±0.7%, and 36.6±1.0%, respectively (**Table 3** and Table S-3 in the Supplemental Material).

Petrographic Data. The coarser siliciclastic beds of the Chang 6 to 8 members are characterized by poor compositional and textural maturity (**Figs. 3 and 4**, Fig. S-1 in the Supplemental Material) and exhibit cross-, horizontal-, parallel-, and wavy-bedding sedimentary structures, including (1) trough and tabular cross-bedding is most common in thick sand bodies (>10 m) **(Fig. S-1c and S-1d)**; (2) wavy and parallel bedding is most common in medium-thick sand bodies (5–10 m) **(Figs. S-1e and S-1f)**; and (3) microwavy and horizontal laminae are most common in thin sand bodies (<5 m) **(Figs. S-1g and S-1h)**. Based on the Folk classification (Folk et al. 1970), the

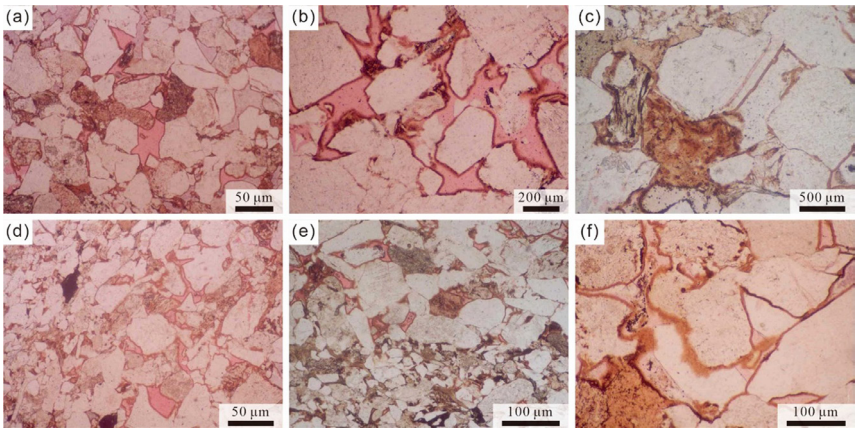

Fig. 4—Selected thin-section photographs (plain-polarized light) showing the microscopic features of siltstones and sandstones with a little or nonoil staining in Chang 6 to 8 members of the Yanchang Formation. (a) Siltstone with intergranular and dissolution pores containing calcite cements, Drillcore ZT-16 at 1714.8 m (Chang 8 Member). (b) Medium-grained sandstone, with edges of quartz grains replaced by calcite, Drillcore ZT-16 at 1714.8 m (Chang 8 Member). (c) Coarse-grained sandstone with quartz overgrowths, Drillcore ZT-16 at 1703.3 m (Chang 8 Member). (d) Siltstone with intergranular and dissolution pores containing calcite cements, Drillcore ZT-16 at 1714.8 m (Chang 8 Member). (e) Very fine-grained sandstone with intergranular and dissolution pores containing calcite cements, Drillcore ZT-16 at 1714.8 m (Chang 8 Member). (f) Fine-grained sandstone with intergranular pores containing calcite cements, Drillcore ZT-16 at 1703.3 m (Chang 8 Member).

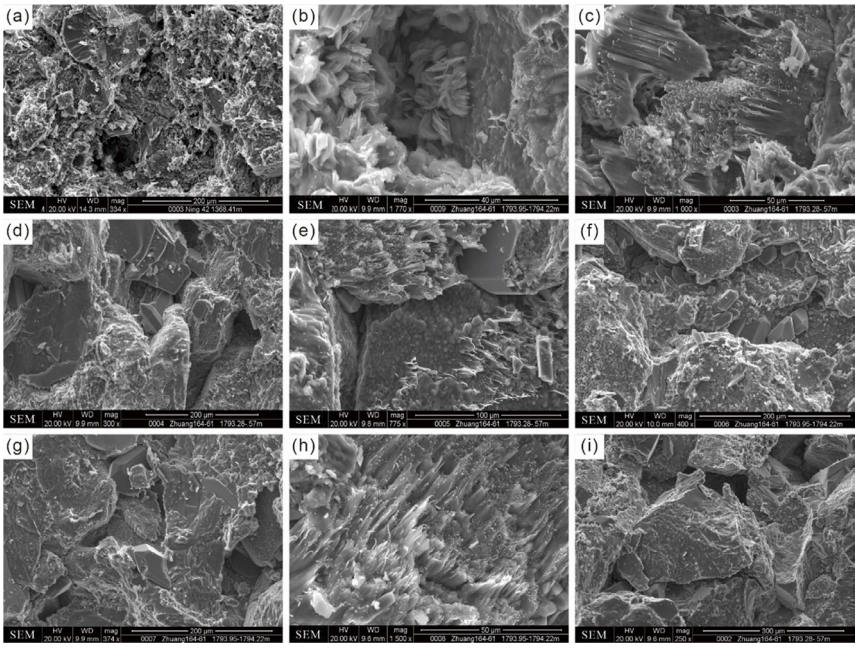

Fig. 5—Selected SEM photographs showing the microscopic features of siltstones and sandstones in Chang 6 to 8 members of the Yanchang Formation. (a) Feldspar particles are dissolved, forming secondary dissolution pores, 334X, Dillcore NT-87 at 1368.4 m (Chang 6 Member). (b) Pores filled with chlorite, 1770X, Drillcore ZT-81 at 1794.0 m (Chang 8 Member). (c) Residual intergranular pores filled with illite clay minerals, 1000X, Drillcore ZT-81 at 1793.3 m (Chang 8 Member). (d) Residual intergranular pores filled with authigenic quartzes, 300X, Drillcore ZT-81 at 1793.3 m (Chang 8 Member). (e) Residual intergranular pores filled with illite clay minerals, 775X, Drillcore ZT-81 at 1793.3 m (Chang 8 Member). (f) Residual intergranular pores filled with authigenic quartzes, 400X, Drillcore ZT-81 at 1794.0 m (Chang 8 Member). (g) Residual intergranular pores filled with authigenic quartzes, 374X, Drillcore ZT-81 at 1794.0 m (Chang 8 Member). (h) Pores filled with illite clay minerals, 1500X, Drillcore ZT-81 at 1794.0 m (Chang 8 Member). (i) Pore-throat features of tight sandstones, 250, Drillcore ZT-81 at 1793.3 m (Chang 8 Member).

siltstones and sandstones comprise feldspathic and quartzose litharenites. The detrital component is dominated by quartz (31.2 to 69.4%, mean 49.7%), feldspar (3.9 to 29.6%, mean 13.5%), and rock fragments (15.7 to 57.9%, mean 36.8%) **(Fig. 9a).** Rock fragments include sedimentary rock fragments (28.6 to 75.2%, mean 52.6%), igneous rock fragments (16.8 to 43.4%, mean 33.9%), and metamorphic rock fragments (2.5 to 29.2%, mean 13.6%) **(Fig. 9b)**. Grains are mostly angular to subrounded **(Figs. 3 and 4)**. Grains exhibit point **(Figs. 3i and 3j)**, flat **(Figs. 3k and 3l)**, and concavo-convex **(Figs. 3a, 3d, and 3f)** contacts. Feldspar and rock fragments show signs of being dissolved partly or in whole **(Figs. 3a, 3c , and 3d)**. The siltstone and sandstone beds consist dominantly of silt-grained particles (43% of beds), followed by very fine-grained particles (25%) and fine-grained particles (22%) **(Fig. 9c)**, and poor grain sorting (39% of beds) is more common than moderate (35%) or good sorting (26%) **(Fig. 9d)**. Note that further petrographic descriptions (e.g., cement features) are given in the section Interpretations.

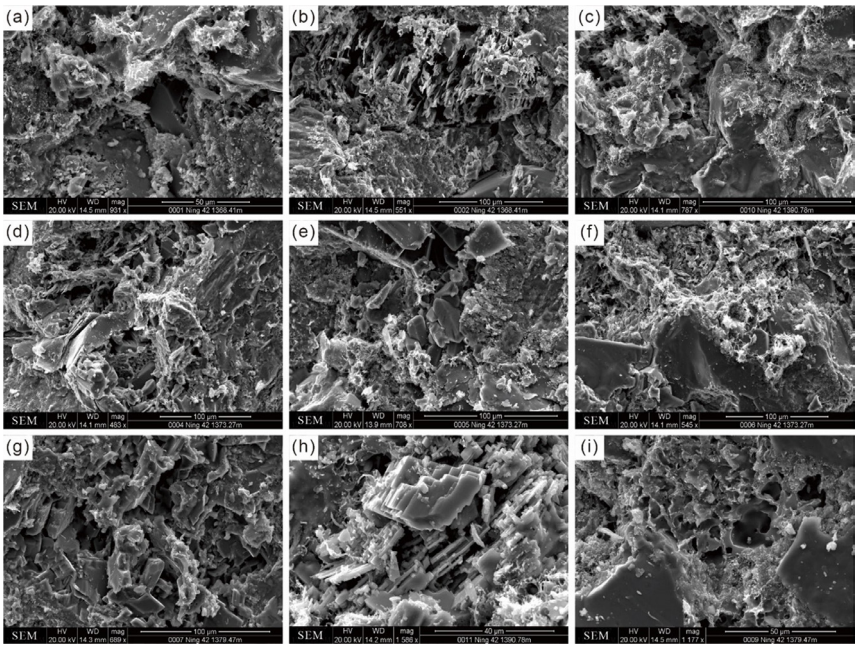

Fig. 6—Selected SEM photographs showing the microscopic features of siltstones and sandstones in Chang 6 to 8 members of the Yanchang Formation. (a) Pores filled with authigenic quartz, kaolinite, and illite, 931X, Drillcore NT-87 at 1368.4 m (Chang 6 Member). (b) Dissolution pores filled with authigenic quartz, 551X, Drillcore NT-87 at 1368.4 m (Chang 6 Member). (c) Dissolution pores filled with illite, 787X, Drillcore NT-87 at 1390.8 m (Chang 6 Member). (d) Dissolution pores filled with authigenic quartz, 483X, Drillcore NT-87 at 1373.3 m (Chang 6 Member). (e) Pores filled with calcite, authigenic albite, and authigenic quartz, 708X, Drillcore NT-87 at 1373.3 m (Chang 6 Member). (f) Pores filled with filamentous illite clay minerals, 545X, Drillcore NT-87 at 1373.3 m (Chang 6 Member). (g) Pores filled with authigenic quartz and ferro-calcite, 689X, Drillcore NT-87 at 1379.5 m (Chang 6 Member). (h) Dissolution pores filled with ankerite, 1586X, Drillcore NT-87 at 1390.8 m (Chang 6 Member). (i) Pores filled with illite clay minerals, 1177X, Drillcore NT-87 at 1379.5 m (Chang 6 Member).

Other Data. ***Cement Content.*** Three kinds of cement are recognized in the study units: (1) clay mineral cements, ranging from 38.6 to 67.3% (mean 52.2%; note all cement values are by volume); (2) carbonate cements, ranging from 26.9 to 46.9% (mean 38.6%); and (3) siliceous cements, ranging from 4.5 to 15.8% (mean 9.2%). For clay mineral cements, a total of four subtypes were recognized: (1a) kaolinite cement, ranging from 4.7 to 52.5% (mean 33.1%); (1b) chlorite cement, ranging from 18.5 to 46.3% (mean 32.5%); (1c) illite cement, ranging from 8.0 to 31.4% (mean 19.7%); and (1d) mixed-layer illite/smectite (I/S) cement, ranging from 0.1 to 32.0% (mean 14.7%) (**Table S-4** and **Fig. S-2** in the Supplemental Material).

$\delta^{13}C$, $\delta^{18}O$, and Paleotemperatures. The carbonate cements yield $\delta^{13}C$ ranging from –14.9 to –3.9% (mean–9.1%) and $\delta^{18}O$ ranging from –27.9 to –17.9% (mean –22.6%) **(Table 4)**. To estimate the paleotemperature of diagenetic fluids, Shackleton (1974) established the following expression:

$$T = 16.9 - 4.38(\delta c - \delta w) + 0.1(\delta c - \delta w)^2, \quad (2)$$

where T is the paleotemperature of the diagenetic fluid in units of °C; δc is the oxygen isotopic ratio of the sample in units of %PDB; and δw is the oxygen isotopic ratio of the diagenetic fluid in units of %SMOW. The oxygen isotopic compositions vary from –20 to –6% (SMOW) because Chang 6 to 8 members were deposited in a continental lacustrine setting, which can accumulate meteoric waters with ^{18}O-depleted isotopic compositions (Xi et al. 2015; Yuan et al. 2015). Assuming a meteoric fluid $\delta^{18}O$ of –7.0±0.6% (SMOW) (Sun et al.

No.	Lithofacies	S_{HGmax}	S_{HGmin}	W_e	D_p	R
1	Siltstones	80.43	64.25	20.18	0.18	3.81
2	Very fine-grained sandstones	82.22	61.91	24.76	0.30	1.88
3	Fine-grained sandstones	78.40	51.92	32.56	0.64	0.85
4	Medium-grained sandstones	83.19	59.38	28.25	1.12	0.52
5	Coarse-grained sandstones	79.26	54.65	31.26	1.68	0.39

*S_{HGmax} = mercury saturation corresponding to the peak pressure on the mercury injection curve, %; S_{HGmin} = mercury saturation corresponding to the minimum pressure on the mercury ejection curve, %; W_e = efficiency of mercury ejection, %; D_p = displacement pressure, MPa; and R = pore-throat radius, μm.

Table 1—The MICP results of reservoirs for five lithofacies in Chang 6 to 8 members of the Yanchang Formation (detailed information is given in Table S-3 of the Supplemental Material).

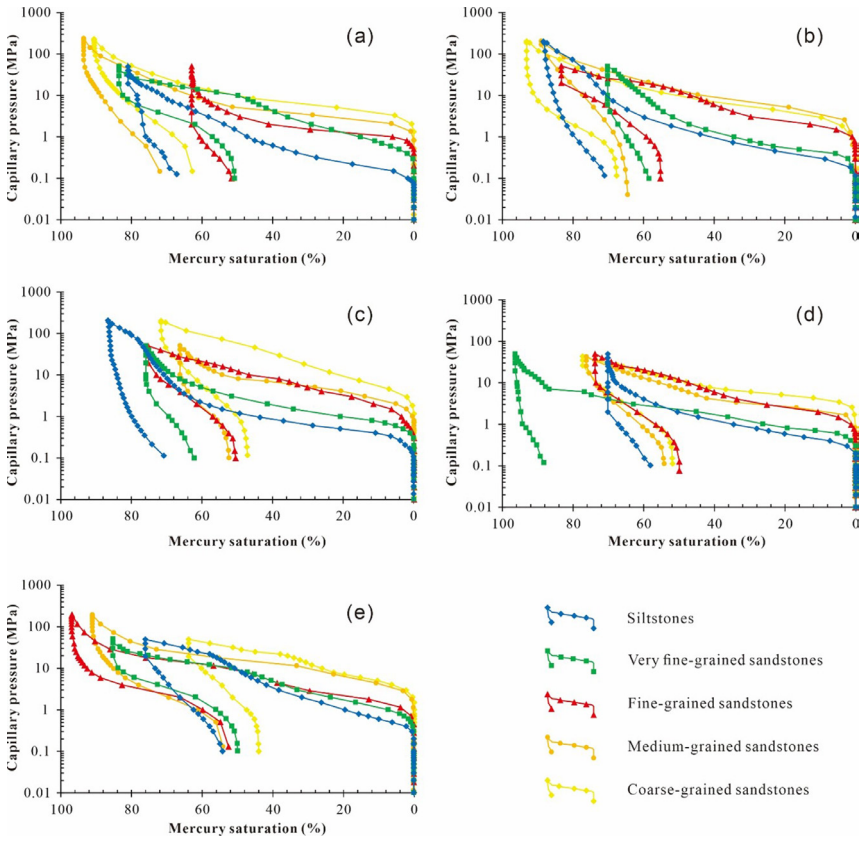

Fig. 7—Capillary pressure curves of reservoirs for five lithofacies in Chang 6 to 8 members of the Yanchang Formation: (a) samples from Drillcore ZT-16; (b) samples from Drillcore ZT-24; (c) samples from Drillcore ZT-57; (d) samples from Drillcore ZT-87; and (e) samples from Drillcore NT-96.

			Porosity (%)			Permeability (md)		
No.	Lithofacies	Samples	Minimum	Maximum	Mean	Minimum	Maximum	Mean
1	Siltstones	*N* = 115	4.02	11.54	8.85	0.0260	0.9383	0.1441
2	Very fine-grained sandstones	*N* = 106	3.48	11.21	8.30	0.0184	0.1900	0.0811
3	Fine-grained sandstones	*N* = 103	1.66	10.71	8.09	0.0138	0.1415	0.0622
4	Medium-grained sandstones	*N* = 93	1.96	10.18	7.67	0.0042	0.1030	0.0483
5	Coarse-grained sandstones	*N* = 85	2.92	9.71	7.45	0.0042	0.0777	0.0434
Mean			–	–	8.12	–	–	0.0792

Table 2—Porosity and permeability of reservoirs for five lithofacies in Chang 6 to 8 members of the Yanchang Formation.

2010), the paleotemperature of the diagenetic fluid from which carbonate cements precipitated in this study ranged from 76.5 to 152.2°C (mean 110.6°C) **(Table 4)**.

Interpretations

Diagenetic Processes. The siltstones and sandstones of the Chang 6 to 8 members experienced complex diagenetic histories after deposition. The main diagenetic processes were compaction, cementation, dissolution, and tectonic fracturing **(Table 5).**

Primary Porosity Destruction. Compaction is a ubiquitous feature of the study units, represented by dewatering structures, deformation, reorientation, and breakage of grains, and dissolution along grain contacts **(Figs. 3 and 4)**. All samples show mechanical and chemical compaction to varying degrees. Three subtypes were recognized based on the degree of compaction: (1) weak compaction, which is most common in thick sand bodies (>10 m) exhibiting largely unmodified point contacts between grains **(Figs. 3i and 3j)**; (2) moderate compaction, which is most common in moderately thick sand bodies (5–10 m) exhibiting flat (i.e., rotated or weakly dissolved) grain contacts **(Figs. 3k and 3l)**; and (3) strong compaction, which is most common in thin sand bodies (<5 m) exhibiting frequent concavo-convex grain contacts **(Figs. 3a, 3d, and 3f)**.

Cementation is also ubiquitous in the study units, with three main types recognized: carbonate, clay mineral, and siliceous cements **(Table 5)**. Clay mineral cements are the most common type (~52% of cements by volume), followed by carbonate (~39%) and siliceous cements (~9%). Carbonate cements mainly consist of calcite **(Fig. 3d)**, ferro-calcite **(Fig. 6g)**, and ankerite **(Fig. 6h)**. These cements mainly form mosaic fabrics in the intergranular dislocations and pores of feldspar, thereby filling the pore space **(Fig. 3g)**. Moreover, thin-section observations by microscopy show that calcite usually replaces the edges of quartz grains **(Fig. 4b)**.

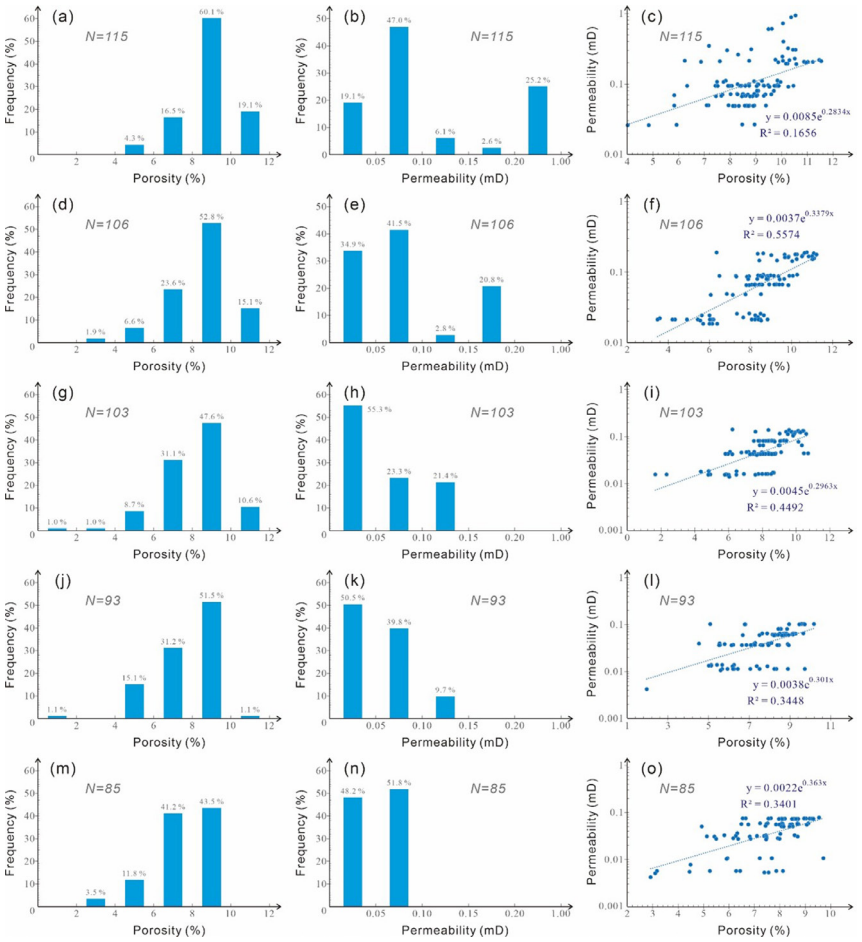

Fig. 8—Distribution of porosity, permeability, and the relationship between porosity and permeability of siltstones and sandstones in Chang 6 to 8 members of the Yanchang Formation: (a-c) siltstones, (d–f) very fine-grained sandstones, (g–i) fine-grained sandstones, (j–l) medium-grained sandstones, and (m–o) Coarse-grained sandstones.

No.	Lithofacies	Samples	S	C_{ci}	C_{cd}	φ_{tp}	φ_{ti}	φ_{ts}	φ_{pc}	φ_{o}	φ_{co}	φ_{ce}	φ_{ed}	φ_{td}	φ_{te}
1	Siltstones	N = 10	1.26	20.90	1.07	2.42	1.66	0.76	7.59	39.11	26.08	21.97	2.42	3.49	1.07
2	Very fine-grained sandstones	N = 10	1.31	19.12	1.09	2.53	1.89	0.64	7.20	38.43	24.37	20.22	1.96	3.05	1.09
3	Fine-grained sandstones	N = 10	1.37	18.56	1.14	2.89	2.11	0.78	8.18	37.64	24.39	19.70	2.36	3.50	1.14
4	Medium-grained sandstones	N = 10	1.42	19.59	1.08	3.33	2.38	0.95	8.42	37.04	25.47	20.68	2.55	3.63	1.08
5	Coarse-grained sandstones	N = 10	1.46	21.15	1.23	1.88	1.44	0.44	6.47	36.57	25.94	22.37	1.68	2.90	1.23
Mean			1.36	19.87	1.12	2.61	1.90	0.71	7.57	37.77	25.25	20.99	2.19	3.31	1.12

S = Trask sorting coefficient; C_{ci} = content of cements within the intergranular pore, %; C_{cd} = content of cements within the dissolution pore, %; φ_{tp} = total thin-section porosity, %; φ_{ti} = thin-section porosity of intergranular pore, %; φ_{ts} = thin-section porosity of dissolution pore, %; φ_{pc} = porosity measured in the core, %; φ_{o} = initial porosity, %; φ_{co} = remaining intergranular porosity following compaction, %; φ_{ce} = total porosity loss caused by cementation, %; φ_{ed} = effective porosity increased by dissolution, %; φ_{td} = total increase in porosity due to dissolution, %; φ_{te} = total increase in porosity due to tectonic fracturing, %.

Table 3—Statistics of porosity evolution parameters of reservoirs for five lithofacies in Chang 6 to 8 members of the Yanchang Formation (detailed information is given in Table S-4 in the Supplemental Material).

Clay mineral cements are primarily composed of kaolinite (~33%), chlorite (~32%), illite (~20%), and mixed-layer I/S (~15%) (**Fig. S-1 and Table S-4** in the Supplemental Material). Illite, kaolinite, and mixed-layer I/S are mainly present in intergranular pores as well as dissolution vugs of feldspar. Kaolinite cements can show vermicular and accordion morphologies. Illite together with mixed-layer I/S grains largely originate from smectite. The illite grains commonly have flaky, fibrous, and honeycomb morphologies **(Fig. 6a)**. On the other hand, authigenic chlorite is a lamellar cement with poor continuity that fills isolated pores or forms grain coatings **(Figs. 3i and 5b)**.

Quartz cements form overgrowths on detrital quartz silt and sand grains **(Fig. 4c)** as well as authigenic quartz crystals **(Fig. 6e)**. Quartz overgrowths on detrital grains fill adjacent intergranular pore spaces. Lines of inclusions mark the contacts between the original detrital grains and their cement overgrowths **(Fig. 4c)**. Authigenic quartz crystals having well-formed facets and sharp crystal edges often fill in

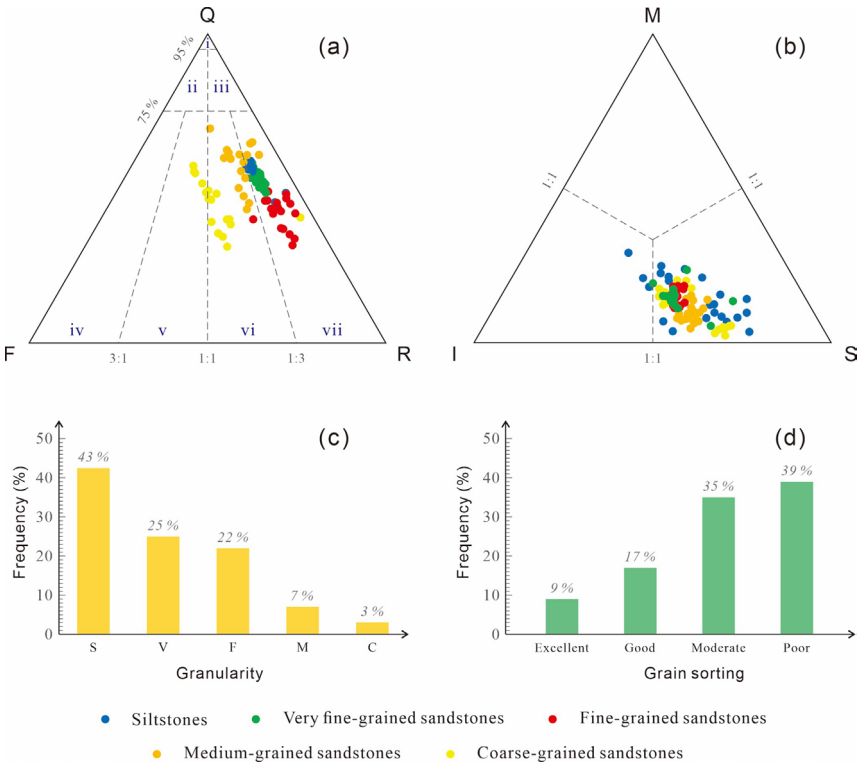

Fig. 9—Rock compositions, rock fragment types, grain-size distributions, and grain sorting in Chang 6 to 8 members of the Yanchang Formation. (a) Scatter graph exhibiting framework grain compositions: Q = monocrystalline and polycrystalline quartz (excluding chert); F = monocrystalline feldspar; R = rock fragments (igneous, metamorphic, and sedimentary; including chert); i = quartzarenite; ii = subfeldsparenite; iii = sublitharenite; iv = feldsparenite; v = lithic feldsparenite; vi = feldspathic litharenite; and vii = litharenite (Folk et al. 1970). (b) Scatter graph exhibiting compositions of rock fragments: M = metamorphic rock fragments; I = igneous rock fragments; and S = sedimentary rock fragments (Folk et al. 1970). (c) Column chart showing the distribution of lithologies related to granularity: S = siltstone (0.0039–0.0625 mm); V = very fine-grained sandstone (0.0625–0.125 mm); F = fine-grained sandstone (0.125–0.25 mm); M = medium-grained sandstone (0.25–0.5 mm); and C = coarse-grained sandstone (0.5–1 mm). (d) Column chart showing the grain sorting.

intergranular pores and dissolutions of feldspar **(Fig. 6e)**. Authigenic quartz is generally found in association with illite **(Fig. 6a)**, calcite **(Fig. 6e)**, authigenic albite **(Fig. 6e)**, and ferro-calcite **(Fig. 6g)**.

Secondary Porosity Creation. Dissolution is a relatively rare diagenetic process in the study units. Selective dissolution of feldspar crystals and rock fragments mainly takes place along cleavage planes in the form of honeycombs or particle edges, resulting in irregular (i.e., harbor-like) dissolution pores. Later, calcite cements always fill them **(Fig. 3a through 3h)**. Based on the results of thin-section observations, the pore-filling carbonate cements were not dissolved.

Tectonic fracturing is not common in the study units, although where present in the HOF it can occur as high-density fracture networks. Most fractures are high-angle (dip >70°), thin (<1 mm wide), and open (i.e., uncemented) **(Fig. S1a)**. In addition, striations on fault planes caused by active movement can also be seen in the rock core **(Fig. S1b)**.

Paragenetic History. The reservoirs went through various post-depositional diagenetic transformations, locally up to the level of incipient metamorphism. In this study, a total of four stages of diagenetic alteration were recognized following the China Petroleum Standard of the Division of Diagenetic Stages in Clastic Rocks (SY/T 5477–2003).

The Penesyngenetic and Eogenetic A Stages are represented by clastic sediments that were buried shallowly (0–1.5 km), reaching maximum burial temperatures of 65°C. The sediments are in a loose to semiconsolidated state and exhibit primary intergranular pores filled with calcite carbonate **(Figs. 3a, 3b, and 3c)** and chlorite clay mineral **(Figs. 3k and 3l)** cements.

The Eogenetic B Stage is represented by clastic sediments that were buried to moderate depths (1.5–2.0 km), reaching maximum burial temperatures of 65 to 85°C. The sediments are in a semiconsolidated to consolidated state due to weak compaction and modest cementation **(Fig. 3i)**. The feldspar grains are partially dissolved **(Fig. 3j)**. With the exception of residual primary intergranular pores, some secondary pores have developed **(Figs. 3i and 3j)**. The minimum paleotemperature of the diagenetic fluid in the study units was 76.5°C **(Table 4)**, which suggests that the siltstones and sandstones have at least undergone the Eogenetic B Stage.

The Early Mesogenetic A Stage is represented by clastic sediments that were buried deeply (2.0–2.5 km), reaching maximum burial temperatures of 85 to 140°C. The sediments are mainly in a consolidated state **(Figs. 3d, 3e, and 3f)**. Feldspar grains and rock fragments were extensively dissolved and developed large secondary pores **(Figs. 3d and 5a)**. Cements of ankerite carbonate **(Fig. 6h)**, clay mineral [illite and mixed-layer I/S **(Figs. 5c, 5e, and 5h)** and kaolinite **(Fig. 6a)**], and siliceous [quartz overgrowth **(Fig. 4c)** and authigenic quartz crystals **(Figs. 5d, 5f, and 5g)**] are present. Drilling data indicate that the current depth of the Chang 6 to 8 members in the study area is 2000±500 m **(Figs. 3 through 6)**. Because denudation since the Late Cretaceous has removed 650±150 m of strata (Liu et al. 2015; Yu et al. 2017), the Chang 6 to 8 members were buried to a depth of 2000 to 3300 m before uplift. This is consistent with estimated paleotemperatures for the diagenetic fluid ranging from 76.5 to 152.2°C **(Table 4)**. These results suggest that some of the siltstones and sandstones have undergone Early Mesogenetic A Stage.

The Late Mesogenetic A Stage is represented by clastic sediments that were buried very deeply (>2.5 km), reaching maximum burial temperatures of 140 to 175°C. The sediments are in a well-consolidated and tight state (low porosity) **(Figs. 3a through 3c, and 8)**.

No.	Drillcore	Member	$\delta^{13}C_{PDB}$ (‰)	$\delta^{18}O_{PDB}$ (‰)	*T*
1	ZT-16	Chang 6	–7.77	–19.04	84.13
2	ZT-16	Chang 6	–6.56	–23.59	117.09
3	ZT-16	Chang 7	–9.82	–25.49	132.07
4	ZT-16	Chang 7	–8.63	–24.73	125.99
5	ZT-16	Chang 8	–9.40	–22.10	105.84
6	ZT-16	Chang 8	–9.10	–23.80	118.71
7	ZT-22	Chang 6	–8.20	–27.40	147.87
8	ZT-22	Chang 6	–5.50	–26.60	141.16
9	ZT-22	Chang 7	–8.00	–21.20	99.26
10	ZT-22	Chang 7	–13.60	–23.10	113.34
11	ZT-22	Chang 8	–8.00	–22.30	107.32
12	ZT-22	Chang 8	–14.40	–17.90	76.52
13	ZT-24	Chang 6	–6.70	–20.18	92.00
14	ZT-24	Chang 6	–5.52	–21.60	102.16
15	ZT-24	Chang 7	–3.87	–18.89	83.12
16	ZT-24	Chang 7	–9.44	–27.31	147.11
17	ZT-24	Chang 8	–12.00	–20.10	91.44
18	ZT-24	Chang 8	–11.93	–21.78	103.48
19	ZT-28	Chang 6	–10.60	–21.43	100.93
20	ZT-28	Chang 6	–9.51	–26.20	137.86
21	ZT-28	Chang 7	–4.24	–22.55	109.19
22	ZT-28	Chang 7	–8.12	–22.88	111.67
23	ZT-28	Chang 8	–7.53	–25.75	134.18
24	ZT-28	Chang 8	–7.33	–19.19	85.15
25	ZT-57	Chang 6	–11.44	–19.00	83.86
26	ZT-57	Chang 6	–10.05	–23.53	116.63
27	ZT-57	Chang 7	–12.30	–22.70	110.32
28	ZT-57	Chang 7	–12.90	–21.60	102.16
29	ZT-57	Chang 8	–8.60	–22.40	108.07
30	ZT-57	Chang 8	–9.48	–21.13	98.76
31	ZT-81	Chang 6	–8.48	–23.22	114.25
32	ZT-81	Chang 6	–8.37	–26.10	137.04
33	ZT-81	Chang 7	–8.89	–26.58	141.00
34	ZT-81	Chang 7	–6.53	–19.40	86.59
35	ZT-81	Chang 8	–9.12	–21.38	100.56
36	ZT-81	Chang 8	–8.40	–19.49	87.21
37	NT-87	Chang 6	–6.56	–21.19	99.19
38	NT-87	Chang 6	–8.13	–24.83	126.79
39	NT-87	Chang 7	–9.30	–23.30	114.86
40	NT-87	Chang 7	–5.70	–24.20	121.82
41	NT-87	Chang 8	–13.40	–27.10	145.34
42	NT-87	Chang 8	–14.90	–18.80	82.51
43	NT-93	Chang 6	–5.72	–20.30	92.84
44	NT-93	Chang 6	–9.84	–27.91	152.21
45	NT-93	Chang 7	–11.63	–21.78	103.48
46	NT-93	Chang 7	–9.71	–26.40	139.51
47	NT-93	Chang 8	–8.12	–22.58	109.41
48	NT-93	Chang 8	–9.63	–19.29	85.83
49	NT-96	Chang 6	–9.05	–23.83	118.94

Table 4—Isotopic compositions of the carbonate cements and calculated temperatures for the cements of siltstones and sandstones in Chang 6 to 8 members of the Yanchang Formation.

No.	Drillcore	Member	$\delta^{13}C_{PDB}$ (‰)	$\delta^{18}O_{PDB}$ (‰)	*T*
50	NT-96	Chang 6	–12.50	–21.60	102.16
51	NT-96	Chang 7	–9.38	–21.83	103.85
52	NT-96	Chang 7	–8.77	–26.20	137.86
53	NT-96	Chang 8	–6.83	–20.50	94.26
54	NT-96	Chang 8	–9.60	–19.39	86.52
Mean			–9.06	–22.64	110.58

T = temperature, °C; $\delta^{18}O_{SMOW}$ = –7±0.

Table 4 (continued)—Isotopic compositions of the carbonate cements and calculated temperatures for the cements of siltstones and sandstones in Chang 6 to 8 members of the Yanchang Formation.

Residual primary intergranular pores as well as secondary pores are filled with ferro-calcite cements **(Fig. 6g)**. In this study, the estimated maximum burial depth is 3300 m **(Figs. 3 through 6)** and the maximum paleotemperature of the diagenetic fluid is 152.2°C **(Table 4)**, which indicates that some of the siltstones and sandstones have experienced Late Mesogenetic A Stage.

Discussion

Depositional Controls on Silty and Sandy Reservoirs. The sedimentary environment regulates the initial distribution of deposited grains and therefore affects evolutionary features during burial diagenesis (Hu et al. 2017; Wang et al. 2017; Hu et al. 2021). The distribution of sand bodies within the Chang 6 to 8 members was controlled by their deposition in braided river delta facies (Wang 2016). The main provenance area for detrital material was the ancient Qingyang Land. This paleoland was located on the southwestern margin of the Yishan Ramp, which formed in the Middle Cambrian and disappeared in the Late Cretaceous. It covered an area of about 3.2×10^3 km^2 during the Late Triassic and was ~15–40 km from the HOF (**Fig. 1b**; Dou et al. 2017).

The braided river delta facies of the study units influenced their rock textures **(Figs. 3 through 4)** and mineral compositions **(Figs. 9a and 9b)** as well as the primary pore systems of the siltstones and sandstones **(Figs. 5 through 6)**. These units exhibit low compositional maturity [i.e., high contents of feldspar **(Figs. 3a and 9a)** and rock debris **(Figs. 3b and 9a)**] and low textural maturity [i.e., mostly angular to subrounded grains **(Figs. 3 and 4)** and moderate to poor grain sorting **(Fig. 9d)**]. These features are an indication of proximal detrital sediment sources and a limited transport distance before final deposition.

Diagenetic Controls on Reservoir Porosity Evolution. Diagenesis controls the porosity evolution and tightness of silty and sandy reservoirs (Zhou et al. 2019; Zvirtes et al. 2020; Dong et al. 2022). Different compositions of carbonate cement can be applied to further constrain when cementation occurred (Liang et al. 2018; Han et al. 2020). The relatively low $\delta^{13}C$ values (–9.06±5.84) suggest that carbon was sourced primarily from the decarboxylation of organic matter (**Table 4**; Ketzer et al. 2003), while the low $\delta^{18}O$ values (–22.64±5.27) reveal that high-temperature conditions may have developed in the siltstones and sandstones of the Chang 6 to 8 members during burial (**Table 4**; Algeo et al. 1992).

Compaction is generally the main diagenetic process governing porosity reduction (Adepehin et al. 2020). Microscopic observations demonstrate that siltstones and sandstones within the Chang 6 to 8 members exhibit moderate to strong compaction, resulting in an irreversible porosity loss **(Figs. 3 and 4)**. These siltstones and sandstones show low-maturity mineral compositions, relatively fine granularity, and poor to moderate sorting **(Figs. 9c and 9d)**, which contribute to moderate to strong compaction. The Chang 6 to 8 members were buried to a maximum depth of 2650±650 m before uplift (Liu et al. 2015; Yu et al. 2017). Moreover, long-term deep burial is likely to have contributed to moderate to strong compaction of these siltstones and sandstones. The degree of porosity loss due to mechanical compaction increases as temperature increases for long periods of time (Worden et al. 2018). During the Cretaceous, the paleogeothermal gradient of the Yanchang Formation reached 4.0°C/100 m (Xu et al. 2017). This may be attributed to the continuous subsidence and thermal events originating from magmatic activities in the deep lithosphere. This relatively high geothermal gradient may have promoted porosity reduction within the reservoir layers of the Chang 6 to 8 members. The remaining intergranular porosity after compaction was mainly filled by cements. Compaction-related porosity changes can be mathematically expressed as:

$$\varphi_{co} = C_{ci} + \varphi_{ti}(\varphi_{pc}/\varphi_{tp}), \quad (3)$$

Diagenetic Processes	Subtypes	Abundance
1. Compaction	–	Ubiquitous
2. Cementation	2.1 Carbonate cementation	Ubiquitous
	2.2 Clay mineral cementation	Ubiquitous
	2.3 Siliceous cementation	Ubiquitous
3. Dissolution	–	Rare
4. Tectonic fracturing	–	Not common

Table 5—Diagenetic processes and their abundance of siltstones and sandstones in Chang 6 to 8 members of the Yanchang Formation

where φ_{co} represents the remaining intergranular porosity following compaction; C_{ci} represents the content of cements within intergranular pores; φ_{ti} represents the thin-section porosity of intergranular pores; φ_{pc} represents the porosity measured in the core; and φ_{tp} represents total thin-section porosity, all in units of %. For the study units, the calculated value of φ_{co} is 25.3±0.9%, and the porosity loss caused by compaction is ~12.5±1.3% **(Table 3)**. The above results demonstrate that compaction is a key diagenetic process influencing reservoir tightness.

Cementation also strongly influences reservoir porosity (Worden et al. 2018). Total cement content is independent of total thin-section porosity, reflecting a complex relationship between these parameters. Total thin-section porosity increases as total cement content increases up to ~8%, and then it declines as total cement content exceeds ~8% (**Fig. S-3a** in the Supplemental Material). The formation of partial cements stabilizes grain packing, thereby retarding further compaction and preserving a degree of porosity (Weibel et al. 2019). The development of a certain amount of cement (up to ~8%) within the Chang 6 to 8 members increased the resistance of the sediments to further compression, thereby slowing compaction. However, as the amount of cement within the connective pore space increased further (e.g., to > ~8%), movement of formation waters (including those rich in organic acids) was reduced, thereby limiting the dissolution of labile grains and formation of reservoir porosity. Furthermore, the amounts of some cement types exhibit inverse relationships with total thin-section porosity values **(Figs. S-3b through S-3f)**, indicating that certain types of cement do not necessarily preserve porosity. Specifically, reservoir quality is effectively reduced by (1) carbonate cements that form blocky or mosaic aggregates that occlude large pores; (2) kaolinite cements with vermicular and accordion morphologies that fill primary and secondary pores, as well as pore throats; (3) fibrous and flaky illite grains that fill pores and pore throats, which are especially detrimental to reservoir quality due to their microporous nature; and (4) chlorite and quartz cements that commonly narrow the diameter of pore throats. Categorization of cements into two main types (i.e., intergranular pore and dissolution pore) allows cement-related porosity loss (φ_{ce}) to be expressed as:

$$\varphi_{ce} = C_{ci} + C_{cd}, \tag{4}$$

where C_{ci} and C_{cd} denote the cement content of intergranular and dissolution pores, respectively, in units of %. For the study units, the calculated value of φ_{ce} is 21.0±1.4% **(Table 3)**, indicating that cementation strongly reduced porosity. Cementation is thus an important diagenetic process contributing to reservoir tightness in the Chang 6 to 8 members of the Yanchang Formation.

Dissolution of soluble mineral particles is the main diagenetic process that generates secondary porosity, thereby enhancing reservoir performance (Valencia and Laya 2020). Feldspars are thermodynamically unstable in the burial environment and are thus commonly the main mineral subject to dissolution and secondary pore formation, although rock fragments can be unstable as well (Limarino et al. 2017). Secondary pores formed through dissolution of feldspars as well as rock fragments can be occluded with later carbonate cements **(Figs. 3h and 3i)**, thereby limiting the effectiveness of secondary porosity development. Hence, the effective porosity enhanced by dissolution (φ_{ed}) is the existing secondary porosity because late cementation does not entirely fill in such pores. So, variation of dissolution-induced porosity (φ_{td}) can be expressed as:

$$\varphi_{td} = \varphi_{ed} + C_{cd}, \tag{5}$$

$$\varphi_{ed} = (\varphi_{ts} / \varphi_{tp})\, \varphi_{pc}, \tag{6}$$

where φ_{ts} is the thin-section porosity of dissolution pores in units of %. For the study units, the calculated values of φ_{ed} and φ_{td} are 2.2±0.5% and 3.3±0.4%, respectively **(Table 3)**.

Tectonic movements produce fractures that can promote hydrocarbon storage and migration (Liang et al. 2016). The Yanshan and Himalayan movements played a vital role in the development of fractures in the Chang 6 to 8 members. The Yanshan Movement was associated with four small-scale uplifts during the Jurassic-Cretaceous and the Himalayan Movement with one large-scale uplift during the Paleogene-Quaternary (Fu et al. 2021). The increases in porosity due to tectonic fracturing (φ_{te}) can be defined as:

$$\varphi_{te} = \varphi_{pc} - (\varphi_{co} - \varphi_{ce} + \varphi_{ed}). \tag{7}$$

For the study units, the calculated value of φ_{te} is 1.1±0.1%.

Paragenetic History of Reservoir Development. The process of reservoir "tightening" (i.e., loss of porosity and permeability) is due to the evolution of porosity together with rock fabrics as burial depth increases and the diagenetic environment changes (Braathen et al. 2018; Gharechelou et al. 2020). To clarify the correlation between porosity evolution and diagenetic sequence, cements can be divided into predissolution as well as post-dissolution cement. The former includes chlorite, micritic calcite, and illite. The post-dissolution cements include quartz overgrowth, authigenic kaolinite, authigenic quartz, ferro-calcite, and ankerite. Petrographic relationships (i.e., sequencing of different features in thin sections) constrain the dating of events to one of the four stages of diagenetic alteration. Grain coatings of thin chlorite are surrounded by micritic calcite cements. Ferro-calcite cements fill secondary dissolution pores **(Figs. 4a through 4d)**. These features suggest that chlorite coatings were produced earliest and then micritic calcite cement, dissolution of detrital feldspars together with rock fragments, and ferro-calcite cements. Quartz overgrowths surround the grain coatings of thin chlorite with poor continuity, and they in turn can be surrounded by ferro-calcite cements **(Fig. 4e)**. These features reveal that chlorite coatings were produced earliest, and then quartz overgrowths followed by ferro-calcite cements. By combining data for burial-thermal conditions (Wang et al. 2017; Zhang et al. 2019), the tightening process of the Chang 6 to 8 members is here considered in the context of four diagenetic stages: (1) Penesyngenetic and Eogenetic A Stage (Late Triassic-Early Jurassic); (2) Eogenetic B Stage (Late Jurassic); (3) Early Mesogenetic A Stage (Early Cretaceous); and (4) Late Mesogenetic A Stage (Late Cretaceous to Recent) **(Fig. 10).** The ages of the diagenetic stages given here are based on petrographic constraints in the context of the burial-depth history of the Yanchang Formation (Wang et al. 2017; Zhang et al. 2019) and should be regarded only as approximate.

1. Penesyngenetic and Eogenetic A Stage: During this stage, the burial depth of the Chang 6 to 8 members was approximately 0 to 1.5 km. The mechanical compaction together with early chlorite cementation **(Fig. 3l)**, as main diagenetic events, triggered porosity changes (Zhang et al. 2019). The siltstones and sandstones in the Chang 6 to 8 members exhibit highly ductile rock fragments **(Fig. 9a)** and moderate to poorly grain sorting **(Fig. 9d)**, resulting in significant compaction during the early burial stage. Concurrently, overburden pressure intensified mechanical compaction, bringing grains closer together as well as turning unconsolidated sediments to semiconsolidated rocks **(Fig. 10)**.
2. Eogenetic B Stage: Reservoir tightening continued through a combination of mechanical along with chemical compaction as well as early cementation [mainly micritic calcite **(Figs. 3a through 3h)**] at burial depths of approximately 1.5 to 2.0 km (Zhang et al.

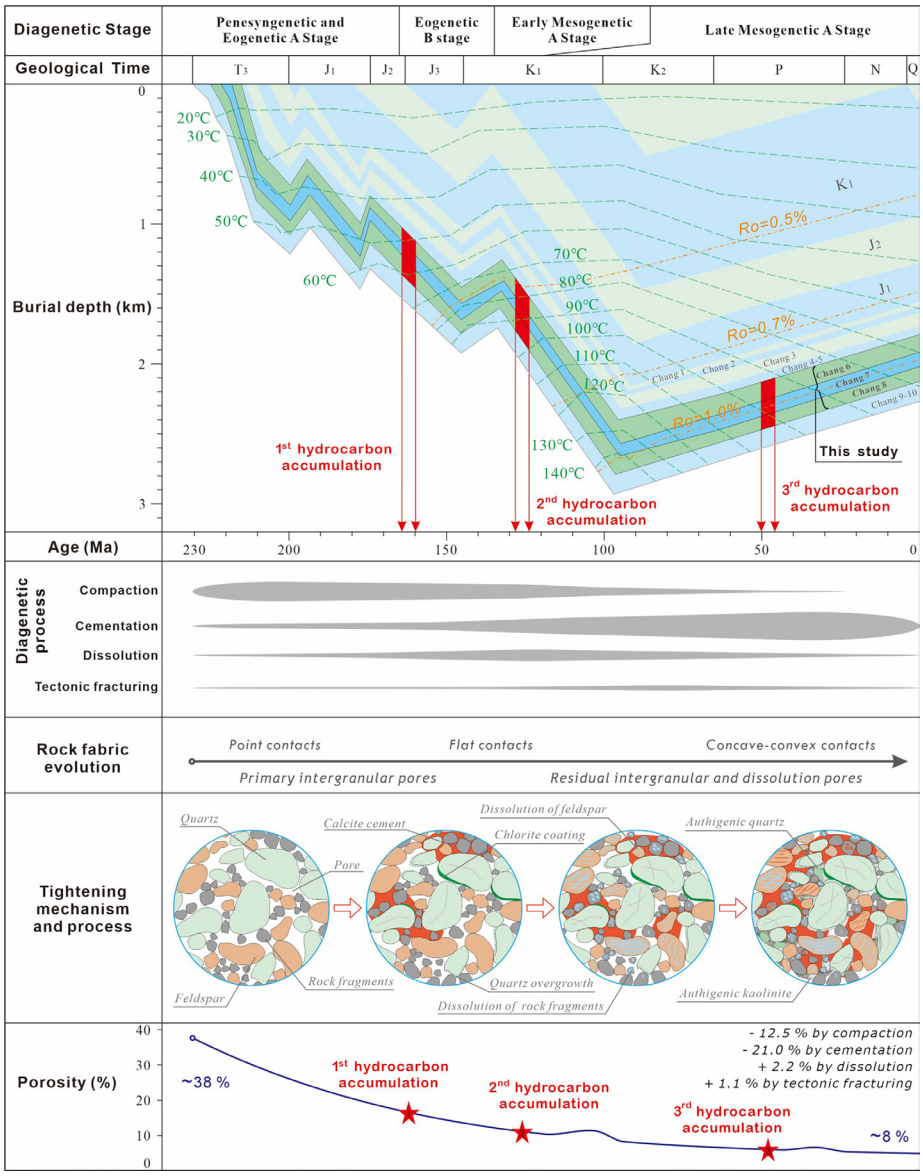

Fig. 10—Comprehensive interpretation diagram for tightening mechanism and processes of siltstones and sandstones in Chang 6 to 8 members of the Yanchang Formation. Burial and thermal evolution history from Wang et al. (2017) and Zhang et al. (2019). Hydrocarbon accumulation episodes from Xi et al. (2008) and Fu et al. (2013): T_3 = Upper Triassic; J_1 = Lower Jurassic; J_2 = Middle Jurassic; J_3 = Upper Jurassic; K_1 = Lower Cretaceous; K_2 = Upper Cretaceous; P = Paleogene; N = Neogene; Q = Quaternary; and *Ro* = vitrinite reflectance.

2019). With the increased buried depth, the intensity of mechanical compaction diagenetic process became heavier as well. The remaining porosity consisted dominantly of primary pores **(Fig. 10)**.

3. Early Mesogenetic A Stage: During this stage, the diagenetic process of mechanical compaction largely ceased. The main diagenetic processes included dissolution of feldspar particles **(Figs. 3a and 5a)** and rock fragments **(Figs. 3b and 3g)** under the influence of organic acid-rich fluids. Moreover, the degree of dissolution was bound up with the migration pathways of organic acid-rich fluids along with the degree of preservation of primary porosity. The organic acids were enriched as well as migrated into the reservoirs of the Chang 6 to 8 members primarily by high-permeability carrier beds, dissolving soluble particles (feldspar as well as rock fragments) and producing secondary pores **(Figs. 3a, 3b and 5a)**, as the maturity of source rocks in the Chang 7 Member increased (**Fig. 10**; Liu et al. 2019; Chen et al. 2020).
4. Late Mesogenetic A Stage: During this stage, the main diagenetic processes included late cementation of authigenic quartz **(Figs. 5d, 5f, and 5g)**, authigenic kaolinite **(Fig. 6a)**, and ferro-calcite **(Fig. 6g)**. Secondary pores were now abundant except for some residual primary porosity **(Figs. 5a, 5g, and 5i)**. Meanwhile, fractures produced by Yanshan and Himalayan movements increased porosity by ~1.1% (**Fig. 10**; Fu et al. 2021).

Summary of Porosity Evolution and Hydrocarbon Charging of Yanchang Formation

The source, reservoir, and cap rocks (SRC association; Snedden et al. 2020) for a petroleum system are well-developed in the Chang 4 to 8 members of the Yanchang Formation. The primary source rocks are shales of the Chang 7 Member having a cumulative thickness of 70±10 m. These shales are mainly characterized by Type I together with Type II_1 kerogen with a mean total organic carbon of 2.2% as well as a mean vitrinite reflectance (*Ro*) of 0.72% (Wang et al. 2017; Xu et al. 2017). The primary reservoir rocks are siltstone and

sandstone within the Chang 6 to 8 members having a cumulative thickness of 185±15 m (80±15 m in Chang 6 Member; 30±5 m in Chang 7 Member; and 75±15 m in Chang 8 Member), exhibiting low porosity (mean 8.1%) and low permeability (mean 0.079 md) (**Fig. 8**; **Table 2**). The cap rocks are mudstones of the Chang 4 to 5 members having a cumulative thickness of 74±5 m (**Fig. 2**; Guo et al. 2014; Zou et al. 2019).

There were three periods of hydrocarbon accumulation in the HOF (Fu et al. 2013; Ding et al. 2019). During the Jurassic, the Chang 6 to 8 members experienced rapid subsidence and a slow temperature increase (subsidence rate = 57.0 m/Myr; temperature rise = 1.3°C/Myr; and geothermal gradient = 2.3°C/100 m). The first period of hydrocarbon charging (193–152 Ma, peaked at ~162 Ma) was initiated at temperatures of ~85°C and resulted in limited filling of reservoirs (Ding et al. 2019). During the Early Cretaceous, the rate of temperature increase began to accelerate (subsidence rate = 37.5 m/Myr; temperature rise = 1.5°C/Myr; and geothermal gradient = 4.0°C/100 m). The second period of hydrocarbon charging (142–120 Ma) represents the main reservoir-filling event. By ~126 Ma, the maximum temperature was 165.0°C and *Ro* was >1.0%, resulting in large-scale maturation and expulsion of hydrocarbons from source rocks (Ding et al. 2019). Since the Late Cretaceous (~96 Ma), the Ordos Basin has experienced polycyclic tectonic uplift with extension faulting around the basin margins, leading to remobilization of earlier hydrocarbon deposits and, thus, the third charging period, which peaked at ~48 Ma (Ding et al. 2019). Evidence of hydrocarbon remobilization is provided by coal-bearing sandstones of Lower-Middle Jurassic age that are bleached and were locally baked through coal combustion and strongly metamorphosed green sandstones of Middle Jurassic age in the southern Yimeng Uplift of the Ordos Basin (**Fig. 1b**; Tan et al. 2017). Based on the relationship between reservoir development and hydrocarbon charging described above, we infer that hydrocarbon accumulation was concurrent with porosity reduction **(Fig. 10)**.

Application of Study Findings to Hydrocarbon Exploration

Reference Framework for Future Exploration of Hydrocarbon Resources in the HOF. Siltstone beds deposited in the delta front environment are the main future exploration targets in the Chang 6 to 8 members of the Upper Triassic Yanchang Formation of the HOF. The results of porosity, permeability, and MICP suggest that siltstone reservoirs (porosity 8.9%; permeability 0.144 md; and pore-throat radius 3.8 μm) are of the best quality, followed by very fine-grained sandstones (porosity 8.3%; permeability 0.081 md; and pore-throat radius 1.9 μm) and fine-grained sandstones (porosity 8.1%; permeability 0.062 md; pore-throat radius 0.9 μm). Medium-grained sandstones (porosity 7.7%; permeability 0.048 md; and pore-throat radius 0.5 μm) and coarse-grained sandstones (porosity 7.5%; permeability 0.043 md; pore-throat radius 0.4 μm) exhibit the worst reservoir quality (**Figs. 7 and 8**; **Tables 1 and 2**).

With regard to sedimentary facies of the Yanchang Formation, the highest quality reservoirs should be located in the delta plain area (e.g., Drillcore ZT-28) because of the development of braided channels (Li et al. 2017; Yang et al. 2021). However, the medium- and coarse-grained sandstones deposited in braided channels exhibit low textural maturity and poor sorting, and compaction during the Penesyngenetic through Eogenetic B stages resulted in substantial loss of porosity from their original value of 36.8% (**Table 3**; Wang et al. 2017), resulting in low-quality reservoirs **(Figs. 8j through 8o)**. In contrast, the siltstones located in the delta front area have a relatively high textural maturity, moderate to good sorting, and an original porosity of 39.1% that was reduced to a more limited degree by burial compaction (**Table 3**; Wang et al. 2017), resulting in relatively high-quality reservoirs **(Figs. 8a, 8b, and 8c)**.

Furthermore, compared with other lithofacies, siltstones are located closer to the mudstone source rocks of the Yanchang Formation, and they make up the largest proportion of deposits by thickness (43%) **(Figs. 2 and 9c)**, providing substantial volume for hydrocarbon accumulation. Therefore, the main future exploration targets should be siltstone beds in the delta front area, such as those in Drillcore ZT-16 at depths of 1443.1 to 1714.8 m (with a total thickness of 121.8 m) as well as in Drillcore NT-93 at depths of 1613.6 to 1884.1 m (with a total thickness of 108.3 m) **(Fig. 1c)**.

Potential Applications to Tight Reservoirs in Other Basins. Nowadays, tight oil resources are found in most parts of the world (Zhang et al. 2017, 2018; Fraser and Pedersen 2021). The exploration and development of tight oil in the United States and Canada has advanced considerably, and the resulting increase in production has reversed the long-term trend of declining oil production in those countries.

One such tight oil play is the Bakken Formation in the Williston Basin (Milliken et al. 2020), which consists of marine clastic deposits (Browne et al. 2020). The Bakken Formation can be divided into three parts: A lower member composed of black shales with a maximum thickness of 15 m; a middle member composed of gray, very fine-grained and fine-grained sandstones, dolomitic sandstones, and siltstones, with a maximum thickness of 26 m; and an upper member composed of black shales with a maximum thickness of 8 m (Novak and Egenhoff 2019; Abdi et al. 2021). The mineral content consists of siliceous clastic minerals (quartz and feldspar) ranging from 30 to 60%, carbonate minerals (calcite and dolomite) ranging from 30 to 80%, and clay minerals (illite, montmorillonite, chlorite, and kaolinite) ranging from 10 to 30% (Barnes et al. 2020; Milliken et al. 2020). The lower and upper members are organic-rich source rocks characterized by Type I and Type II kerogen, with a mean total organic carbon of 11.3% and a mean *Ro* of 0.8% (Halabura et al. 2007; Abdi et al. 2021). Porosity in the tight reservoirs consists of residual intergranular pores, dissolution pores, and locally developed fractures, which are formed mainly in the dolomite-argillaceous siltstones of the middle member (Milliken et al. 2020). Porosity ranges from 5 to 10%, permeability ranges from 0.01 to 0.10 md, and pore-throat radii range from 0.01 to 0.50 μm (Milliken et al. 2020). The Bakken Formation of the Williston Basin thus has strong similarities to the Chang 6 to 8 members of the Yanchang Formation in the Ordos Basin with regard to lithologies, formation properties, and stratal patterns. The present study may therefore provide insights into the evolution of similarly tight reservoirs in other basins.

Conclusions

The Chang 6 to 8 members of the Upper Triassic Yanchang Formation in the HOF, southwestern Ordos Basin, record development of silty and sandy reservoirs suitable for hydrocarbon accumulation. The reservoirs are present in braided river delta plain and delta front facies that accumulated sediments of low compositional and textural maturity. In the burial environment, they underwent a complex diagenetic history that reduced porosity from an initial average of ~38% to the present ~8%. Porosity-destructive processes included compaction (~ –12.5%) and cementation (~ –21 %), with increases in porosity related to grain dissolution (~ +2.2%) and tectonic fracturing (~ +1.1%).

The reservoirs of the Chang 6 to 8 members underwent four post-depositional diagenetic stages: (1) Penesyngenetic and Eogenetic A Stage (Late Triassic-Early Jurassic); (2) Eogenetic B Stage (Late Jurassic); (3) Early Mesogenetic A Stage (Early Cretaceous); and (4) Late Mesogenetic A Stage (Late Cretaceous to Recent). Hydrocarbon charging of these reservoirs occurred in three pulses. Ambient pore space was partly filled by hydrocarbons during the Eogenetic B Stage. A second hydrocarbon charging event occurred during the Early Mesogenetic A Stage, when residual primary intergranular pores as well as secondary dissolution pores were filled. A third hydrocarbon charging event occurred during the Late Mesogenetic A Stage, when the reservoirs were tight. Siltstone beds deposited in delta front environments are the main future exploration targets in the Chang 6 to 8 members. The results of this study provide a useful reference

framework for future exploration of hydrocarbon resources in the Upper Triassic Yanchang Formation of the HOF as well as potential insights into the evolution of similarly tight reservoirs in other basins.

Acknowledgments

Thanks to Petrochina Changqing Oilfield Company and Beijing Ainengtaike Technology Co., LTD for providing data. We thank Weishao Tong, Xuliang Wang, Wenxuan Sun, and Qiuxia Yuan for their help in data analysis. This study was supported by Natural Science Foundation of Xinjiang Uygur Autonomous Region (2020D01C064; 2020D01C037) and Natural Science Foundation of China (42062010). Thanks are also extended to SPE Reservoir Evaluation & Engineering-Formation Evaluation Executive Editor Silviu Livescu and four anonymous reviewers for their constructive comments.

References

Abdi, Z., Rimmer, S. M., Rowe, H. D. et al. 2021. Controls on Organic Matter Accumulation in the Bakken Formation, Williston Basin, USA. *Chem Geol* **586**: 120588. https://doi.org/10.1016/j.chemgeo.2021.120588.

Abrajevitch, A. 2020. Diagenetic Formation of Bedded Chert: Implications from a Rock Magnetic Study of Siliceous Precursor Sediments. *Earth and Planetary Sci Lett* **533**. https://doi.org/10.1016/j.epsl.2019.116039.

Adepehin, E. J., Ali, C. A., Zakaria, A. A. et al. 2020. Post-Depositional Controls on Siliciclastic Tight Reservoirs: Implications from the Oligocene Nyalau Formation (Cycle 1), Onshore Central Sarawak, Borneo. *Mar Pet Geol* **111**: 786–806. https://doi.org/10.1016/j.marpetgeo.2019.09.004.

Algeo, T. J., Wilkinson, B. H., and Lohmann, K. C. 1992. Meteoric-Burial Diagenesis of Middle Pennsylvanian Limestones in the Orogrande Basin, New Mexico: Water/Rock Interactions and Basin Geothermics. *SEPM JSR* **62** (4): 652–670. https://doi.org/10.1306/D426797E-2B26-11D7-8648000102C1865D.

Amosu, A., Imsalem, M., and Sun, Y. 2021. Effective Machine Learning Identification of TOC-Rich Zones in the Eagle Ford Shale. *J Appl Geophy* **188**: 104311. https://doi.org/10.1016/j.jappgeo.2021.104311.

Barnes, B. D., Husson, J. M., Peters, S. E. et al. 2020. Authigenic Carbonate Burial in the Late Devonian–Early Mississippian Bakken Formation (Williston Basin, USA). *Sedimentology* **67** (4): 2065–2094. https://doi.org/10.1111/sed.12695.

Beard, D. C. and Weyl, P. K. 1973. Influence of Texture on Porosity and Permeability of Unconsolidated Sand. *AAPG Bulletin* **57** (2): 349–369. https://doi.org/10.1306/819A4272-16C5-11D7-8645000102C1865D.

Braathen, A., Midtkandal, I., Mulrooney, M. J. et al. 2018. Growth-Faults from Delta Collapse - Structural and Sedimentological Investigation of the Last Chance Delta, Ferron Sandstone, Utah. *Basin Res* **30** (4): 688–707. https://doi.org/10.1111/bre.12271.

Browne, T. N., Hofmann, M. H., Malkowski, M. A. et al. 2020. Redox and Paleoenvironmental Conditions of the Devonian-Carboniferous Sappington Formation, Southwestern Montana, and Comparison to the Bakken Formation, Williston Basin. *Palaeogeography, Palaeoclimatology, Palaeoecology* **560**: 110025. https://doi.org/10.1016/j.palaeo.2020.110025.

Busch, B., Becker, I., Koehrer, B. et al. 2019. Porosity Evolution of Two Upper Carboniferous Tight-Gas-Fluvial Sandstone Reservoirs: Impact of Fractures and Total Cement Volumes on Reservoir Quality. *Mar Pet Geol* **100**: 376–390. https://doi.org/10.1016/j.marpetgeo.2018.10.051.

Cao, J. J., Yang, Y. Y., Chen, C. B. et al. 2019. Analysis of Configuration Characteristics for Skeleton Sand Body with Tight Sandstone Reservoir: A Case Study of Triassic Chang 6 Member in Heshui Area, Ordos Basin, NW China (in Chinese). *Acta Sedimentlologica Sinica* **37** (6): 1005–1116.

Chang, J., Qiu, N., Liu, S. et al. 2019. Post-Triassic Multiple Exhumation of the Taihang Mountains Revealed via Low-T Thermochronology: Implications for the Paleo-Geomorphologic Reconstruction of the North China Craton. *Gondwana Research* **68**: 34–49. https://doi.org/10.1016/j.gr.2018.11.007.

Chen, Y., Lin, S., Bai, B. et al. 2020. Effects of Petroleum Retention and Migration within the Triassic Chang 7 Member of the Ordos Basin, China. *Int J Coal Geol* **225**: 103502. https://doi.org/10.1016/j.coal.2020.103502.

Cohen, K. M., Finney, S. C., Gibbard, P. L. et al. 2013. The ICS International Chronostratigraphic Chart. *Episodes* **36** (3): 199–204. https://doi.org/10.18814/epiiugs/2013/v36i3/002.

Deng, X. Q., Liu, X. S., and Li, S. X. 2009. The Relationship between Compacting History and Hydrocarbon Accumulating History of the Super-Low Permeability Reservoirs in the Triassic Yanchang Formation in the Ordos Basin (in Chinese). *Oil & Gas Geology* **30** (2): 156–161.

Ding, C., Guo, S., Guo, L. et al. 2019. Hydrocarbon Charging Time of Chang 8 Reservoir of Yanchang Formation in Southern Ordos Basin (in Chinese). *Lithologic Reservoirs* **31** (4): 21–31.

Dong, L., Han, C., Santosh, M. et al. 2022. Factors Influencing the Pore Structure and Gas-Bearing Characteristics of Shales: Insights from the Longmaxi Formation, Southern Sichuan Basin and Northern Yunnan-Guizhou Depression, China. *Geofluids* **2022**: 1–20. https://doi.org/10.1155/2022/1692516.

Donohue, C. M. and Barrie, C. D. 2021. A Review of the Bakken Petroleum Systems in the United States and Canada: Recognizing the Importance of the Middle Member Play. *Bulletin* **105** (9): 1847–1866. https://doi.org/10.1306/04122120093.

Dou, W. C., Liu, L. F., Wu, K. J. et al. 2018. Diagenesis of Tight Oil Sand Reservoirs: Upper Triassic Tight Sandstones of Yanchang Formation in Ordos Basin, China. *Geological Journal* **53** (2): 707–724. https://doi.org/10.1002/gj.2922.

Dou, W., Liu, L., Wu, K. et al. 2017. Origin and Significance of Secondary Porosity: A Case Study of Upper Triassic Tight Sandstones of Yanchang Formation in Ordos Basin, China. *J Pet Sci Eng* **149**: 485–496. https://doi.org/10.1016/j.petrol.2016.10.057.

Ettinger, N. P., Larson, T. E., Kerans, C. et al. 2021. Ocean Acidification and Photic-zone Anoxia at the Toarcian Oceanic Anoxic Event: Insights from the Adriatic Carbonate Platform. *Sedimentology* **68** (1): 63–107. https://doi.org/10.1111/sed.12786.

Fall, A., Eichhubl, P., Bodnar, R. J. et al. 2015. Natural Hydraulic Fracturing of Tight-Gas Sandstone Reservoirs, Piceance Basin, Colorado. *Geological Society of America Bulletin* **127** (1–2): 61–75. https://doi.org/10.1130/B31021.1.

Folk, R. L., Andrews, P. B., and Lewis, D. W. 1970. Detrital Sedimentary Rock Classification and Nomenclature for Use in New Zealand. *New Zealand Journal of Geology and Geophysics* **13** (4): 937–968. https://doi.org/10.1080/00288306.1970.10418211.

Fraser, J. A. and Pedersen, P. K. 2021. Reservoir Characterization of Fairways in a Tight Light Oil Play of the Upper Cretaceous Cardium Formation, West Pembina, Alberta, Canada. *Bulletin* **105** (9): 1797–1820. https://doi.org/10.1306/06032120131.

Fu, J. H., Liu, G. D., Yang, W. W. et al. 2013. A Study of the Accumulation Periods of Low Permeability Reservoir of Yanchang Formation in Longdong Area, Ordos Basin (in Chinese). *Earth Science Frontiers* **20** (2): 125–131.

Fu, L., Li, J., Xu, W. et al. 2021. Characteristics and Main Controlling Factors of Ordovician Deep Subsalt Reservoir in Central and Eastern Ordos Basin, China. *J Nat Gas Geosci* **6** (1): 13–25. https://doi.org/10.1016/j.jnggs.2021.03.001.

Gao, H., Zhugeng, B. L., Wang, X. Y. et al. 2019. Differences and Origin of Micro-Pore Throat Characteristics for Tight Sandstone Reservoir of Yanchang Formation, Ordos Basin (in Chinese). *Oil and Gas Geology* **40** (2): 302–312.

Gharechelou, S., Amini, A., Bohloli, B. et al. 2020. Distribution of Geomechanical Units Constrained by Sequence Stratigraphic Framework: Useful Data Improving Reservoir Characterization. *Mar Pet Geol* **117**: 104398. https://doi.org/10.1016/j.marpetgeo.2020.104398.

Gu, Y., Zhang, D., Lin, Y. et al. 2021. Data-Driven Lithology Prediction for Tight Sandstone Reservoirs Based on New Ensemble Learning of Conventional Logs: A Demonstration of A Yanchang Member, Ordos Basin. *J Pet Sci Eng* **207**. https://doi.org/10.1016/j.petrol.2021.109292.

Guo, H., He, R., Jia, W. et al. 2018. Pore Characteristics of Lacustrine Shale within the Oil Window in the Upper Triassic Yanchang Formation, Southeastern Ordos Basin, China. *Mar Pet Geol* **91**: 279–296. https://doi.org/10.1016/j.marpetgeo.2018.01.013.

Guo, H., Jia, W., Peng, P. et al. 2014. The Composition and Its Impact on the Methane Sorption of Lacustrine Shales from the Upper Triassic Yanchang Formation, Ordos Basin, China. *Mar Pet Geol* **57**: 509–520. https://doi.org/10.1016/j.marpetgeo.2014.05.010.

Halabura, S., Buatois, L., Angulo, S. et al. 2007. From Source to Trap: A Review of the Bakken Petroleum System, Upper Devonian-Mississip-Pian, Southeastern Saskatchewan. Summary of Investigations, Saskatchewan Geological Survey, Saskatchewan, Canada.

Han, C. C., Tian, J. J., Hu, C. L. et al. 2020. Lithofacies Characteristics and Their Controlling Effects on Reservoirs in Buried Hills of Metamorphic Rocks: A Case Study of Late Paleozoic Units in the Aryskum Depression, South Turgay Basin, Kazakhstan. *J Pet Sci Eng* **191**: 107137. https://doi.org/10.1016/j.petrol.2020.107137.

He, C., Ji, L., Su, A. et al. 2019. Source-Rock Evaluation and Depositional Environment of Black Shales in the Triassic Yanchang Formation, Southern Ordos Basin, North-Central China. *J Pet Sci Eng* **173**: 899–911. https://doi.org/10.1016/j.petrol.2018.10.089.

Hu, C. L., Zhang, Y. F., Jiang, Z. X. et al. 2020a. Tectonic and Paleogeographic Controls on Development of the Early–Middle Ordovician Shanganning Carbonate Platform, Ordos Basin, North China. *AAPG Bulletin* **104** (3): 565–593. https://doi.org/10.1306/06121918175.

Hu, C. L., Zhang, Y. F., Jiang, Z. X. et al. 2021. Development of Large-scale Sand Bodies in a Fault-bounded Lake Basin: Pleistocene-Holocene Poyang Lake, Southern China. *J Paleolimnol* **65** (4): 407–428. https://doi.org/10.1007/s10933-021-00179-9.

Hu, C. L., Zhang, Y. F., Tian, J. J. et al. 2020b. Influence of Paleo-Trade Winds on Facies Patterns of the Cambrian Shanganning Carbonate Platform, North China. *Palaeogeography, Palaeoclimatology, Palaeoecology* **552**. https://doi.org/10.1016/j.palaeo.2019.109556.

Hu, C., Zhang, Y., Feng, D. et al. 2017. Flume Tank Simulation on Depositional Mechanism and Controlling Factors of Beach-Bar Reservoirs. *J Earth Sci* **28** (6): 1153–1162. https://doi.org/10.1007/s12583-016-0929-4.

Jiang, Z. X., Xu, J., and Wang, G. T. 2012. The Discovery and Significance of a Sedimentary Hiatus within the Carboniferous Taiyuan Formation, Northeastern Ordos Basin, China. *Bulletin* **96** (7): 1173–1195. https://doi.org/10.1306/11021111073.

Ji, L., Meng, F., Schiffbauer, J. D. et al. 2008. Correlation between Highly Abundant Oil-Prone Leiosphaerid Acritarchs and Hydrocarbon Source Rocks from the Triassic Yanchang Formation, Eastern Gansu Province, Northwestern China. *Gondwana Research* **14** (3): 554–560. https://doi.org/10.1016/j.gr.2008.04.006.

Ji, L. M., Li, J. F., and Song, Z. G. 2009. Petroleum Geological Significance of Botryococcus in Triassic Yanchang Formation, Ordos Basin (in Chinese). *Pet Explor Dev* **36** (2): 156–165.

Kassem, A. A., Hussein, W. S., Radwan, A. E. et al. 2021. Petrographic and Diagenetic Study of Siliciclastic Jurassic Sediments from the Northeastern Margin of Africa: Implication for Reservoir Quality. *J Pet Sci Eng* **200**: 108340. https://doi.org/10.1016/j.petrol.2020.108340.

Ketzer, J. M., Holz, M., Morad, S. et al. 2003. Sequence Stratigraphic Distribution of Diagenetic Alterations in Coal-Bearing, Paralic Sandstones: Evidence from the Rio Bonito Formation (Early Permian), Southern Brazil. *Sedimentology* **50** (5): 855–877. https://doi.org/10.1046/j.1365-3091.2003.00586.x.

Lai, J., Fan, X., Liu, B. et al. 2020. Qualitative and Quantitative Prediction of Diagenetic Facies via Well Logs. *Mar Pet Geol* **120**: 104486. https://doi.org/10.1016/j.marpetgeo.2020.104486.

Li, Q., Wu, S., Xia, D. et al. 2020. Major and Trace Element Geochemistry of the Lacustrine Organic-Rich Shales from the Upper Triassic Chang 7 Member in the Southwestern Ordos Basin, China: Implications for Paleoenvironment and Organic Matter Accumulation. *Mar Pet Geol* **111**: 852–867. https://doi.org/10.1016/j.marpetgeo.2019.09.003.

Li, Z., Wu, S., Xia, D. et al. 2017. Diagenetic Alterations and Reservoir Heterogeneity within the Depositional Facies: A Case Study from Distributary-Channel Belt Sandstone of Upper Triassic Yanchang Formation Reservoirs (Ordos Basin, China). *Mar Pet Geol* **86**: 950–971. https://doi.org/10.1016/j.marpetgeo.2017.07.002.

Liang, C., Cao, Y., Liu, K. et al. 2018. Diagenetic Variation at the Lamina Scale in Lacustrine Organic-Rich Shales: Implications for Hydrocarbon Migration and Accumulation. *Geochim Cosmochim Acta* **229**: 112–128. https://doi.org/10.1016/j.gca.2018.03.017.

Liang, C., Jiang, Z., Cao, Y. et al. 2016. Deep-Water Depositional Mechanisms and Significance for Unconventional Hydrocarbon Exploration: A Case Study from the Lower Silurian Longmaxi Shale in the Southeastern Sichuan Basin. *Bulletin* **100** (05): 773–794. https://doi.org/10.1306/02031615002.

Limarino, C. O., Giordano, S. R., and Rodriguez Albertani, R. J. 2017. Diagenetic Model of the Bajo Barreal Formation (Cretaceous) in the Southwestern Flank of the Golfo de San Jorge Basin (Patagonia, Argentina). *Mar Pet Geol* **88**: 907–931. https://doi.org/10.1016/j.marpetgeo.2017.09.024.

Lin, H. B., Hou, M. C., Chen, H. D. et al. 2008. Characteristics and Evolution of the Sedimentary System of Upper Triassic Yanchang Formation in Ordos Basin, China (in Chinese). *Journal of Chengdu University of Technology (Science and Technology Edition)* **35** (6): 674–680.

Liu, D. Y., Li, H. C., Zhang, C. et al. 2019. Experimental Investigation of Pore Development of the Chang 7 Member Shale in the Ordos Basin under Semi-Closed High-Pressure Pyrolysis. *Mar Pet Geol* **99**: 17–26. https://doi.org/10.1016/j.marpetgeo.2018.08.014.

Liu, Q. Y., Jin, Z. J., Meng, Q. Q. et al. 2015. Genetic Types of Natural Gas and Filling Patterns in Daniudi Gas Field, Ordos Basin, China. *J Asian Earth Sci* **107**: 1–11. https://doi.org/10.1016/j.jseaes.2015.04.001.

Ma, H. 2017. Evaluation of Elastic Dissolved Gas Drive in Chang 7 Reservoir Development Adaptability Evaluation (in Chinese). *Oil and Gas Production* **43** (7): 55.

Mehrabi, H., Bahrehvar, M., and Rahimpour-Bonab, H. 2021. Porosity Evolution in Sequence Stratigraphic Framework: A Case from Cretaceous Carbonate Reservoir in the Persian Gulf, Southern Iran. *J Pet Sci Eng* **196**: 107699. https://doi.org/10.1016/j.petrol.2020.107699.

Milliken, K. L., Zhang, T., Chen, J. et al. 2020. Mineral Diagenetic Control of Expulsion Efficiency in Organic-Rich Mudrocks, Bakken Formation (Devonian-Mississippian), Williston Basin, North Dakota, U.S.A. *Mar Pet Geol* **127**: 104869. https://doi.org/10.1016/j.marpetgeo.2020.104869.

Novak, A. and Egenhoff, S. 2019. Soft-Sediment Deformation Structures as a Tool to Recognize Synsedimentary Tectonic Activity in the Middle Member of the Bakken Formation, Williston Basin, North Dakota. *Mar Pet Geol* **105**: 124–140. https://doi.org/10.1016/j.marpetgeo.2019.04.012.

Orlov, D., Ebadi, M., Muravleva, E. et al. 2021. Different Methods of Permeability Calculation in Digital Twins of Tight Sandstones. *J Nat Gas Sci Eng* **87**: 103750. https://doi.org/10.1016/j.jngse.2020.103750.

Radwan, A. E., Trippetta, F., Kassem, A. A. et al. 2021. Multi-Scale Characterization of Unconventional Tight Carbonate Reservoir: Insights from October Oil Filed, Gulf of Suez Rift Basin, Egypt. *J Pet Sci Eng* **197**: 107968. https://doi.org/10.1016/j.petrol.2020.107968.

Ran, Y., Wang, G. W., Lai, J. et al. 2016. Quantitative Characterization of Diagenetic Facies of Tight Sandstone Oil Reservoir by Using Logging Crossplot: A Case Study on Chang 7 Tight Sandstone Oil Reservoir in Huachi Area, Ordos Basin (in Chinese). *Acta Sedimentologica Sinica* **34** (4): 694–706.

Rashid, F., Glover, P. W. J., Lorinczi, P. et al. 2015. Porosity and Permeability of Tight Carbonate Reservoir Rocks in the North of Iraq. *J Pet Sci Eng* **133**: 147–161. https://doi.org/10.1016/j.petrol.2015.05.009.

Ren, D., Zhou, D., Liu, D. et al. 2019. Formation Mechanism of the Upper Triassic Yanchang Formation Tight Sandstone Reservoir in Ordos Basin—Take Chang 6 Reservoir in Jiyuan Oil Field as an Example. *J Pet Sci Eng* **178**: 497–505. https://doi.org/10.1016/j.petrol.2019.03.021.

Sadeghi, R., Moussavi-Harami, R., kadkhodaie, A. et al. 2021. Reservoir Rock Typing of the Asmari Formation Using Integrating Geological and Petrophysical Data for Unraveling the Reservoir Heterogeneity: A Case Study from the Ramshir Oilfield, Southwest Iran. *Carbonates Evaporites* **36** (3): 1–28. https://doi.org/10.1007/s13146-021-00692-y.

Sanguinito, S., Cvetic, P., Goodman, A. et al. 2020. Characterizing Pore-Scale Geochemical Alterations in Eagle Ford and Barnett Shale from Exposure to Hydraulic Fracturing Fluid and CO_2/H_2O. *Energy Fuels* **35** (1): 583–598. https://doi.org/10.1021/acs.energyfuels.0c02496.

Scherer, M. 1987. Parameters Influencing Porosity in Sandstones: A Model for Sandstone Porosity Prediction: ERRATUM. *AAPG Bulletin* **71** (5): 485–491. https://doi.org/10.1306/703C80FB-1707-11D7-8645000102C1865D.

Shackleton, N. J. 1974. Attainment of Isotopic Equilibrium between Ocean Water and the Benthonic Foraminifera Genus Uvigerina: Isotopic Changes in the Ocean during the Last Glacial. Paper presented at the In Proceedings of the Colloques Internationaux Du Centre National de La Recherche Scientifique No, 219, 203–209, Paris, France: Colloques Internationaux du Centre National de la Recherche Scientifique.

Shi, J., Wan, X., Xie, Q. et al. 2021. Difference of Microfeatures among Diagenetic Facies in Tight Sandstone Reservoirs of the Triassic Yanchang Formation in the Midwestern Region, Ordos Basin. *Math Probl Eng* **2021**: 1–11. https://doi.org/10.1155/2021/5611786.

Snedden, J. W., Cunningham, R. C., and Virdell, J. W. 2020. The Northern Gulf of Mexico Offshore Super Basin: Reservoirs, Source Rocks, Seals, Traps, and Successes. *Bulletin* **104** (12): 2603–2642. https://doi.org/10.1306/09092020054.

Suboyin, A., Rahman, M. M., and Haroun, M. 2020. Hydraulic Fracturing Design Considerations, Water Management Challenges and Insights for Middle Eastern Shale Gas Reservoirs. *Energy Reports* **6**: 745–760. https://doi.org/10.1016/j.egyr.2020.03.017.

Sun, Z. X., Sun, Z. L., Lu, H. J. et al. 2010. Characteristics of Carbonate Cements in Sandstone Reservoirs: A Case from Yanchang Formation, Middle and Southern Ordos Basin, China. *Pet Explor Dev* **37** (5): 543–551. https://doi.org/10.1016/S1876-3804(10)60054-7.

Syah, R., Alizadeh, S. M., Nasution, M. K. M. et al. 2021. Carbon Dioxide-Based Enhanced Oil Recovery Methods to Evaluate Tight Oil Reservoirs Productivity: A Laboratory Perspective Coupled with Geo-Sequestration Feature. *Energy Reports* **7**: 4697–4704. https://doi.org/10.1016/j.egyr.2021.07.043.

Syed, F. I., Alnaqbi, S., Muther, T. et al. 2021. Smart Shale Gas Production Performance Analysis Using Machine Learning Applications. *Petroleum Research* **7** (1): 21–31. https://doi.org/10.1016/j.ptlrs.2021.06.003.

Tan, Y. H., Wang, J. Q., Gao, D. et al. 2017. Alteration Characteristics and Genetic Mechanisms of Yan'an Formation Sandstone Bleaching in Dongsheng Area. *Natural Gas Exploration and Development* **40** (4): 17–24. https://doi.org/10.12055/gaskk.issn.1673-3177.2017.04.003.

Tian, Y. M., Shi, Z. J., Song, J. H. et al. 2011. Diagenesis Characteristics of the Chang 8 - Chang 6 Members of Yanchang Formation in Yichuan-Xunyi Area, Ordos Basin (in Chinese). *Journal of Southwest Petroleum University (Science and Technology Edition)* **33** (4): 44–52.

Uzun, O. and Kazemi, H. 2021. Assessment of Enhanced Oil Recovery by Osmotic Pressure in Unconventional Reservoirs: Application to Niobrara Chalk and Codell Sandstone. *Fuel* **306**: 121270. https://doi.org/10.1016/j.fuel.2021.121270.

Valencia, F. L. and Laya, J. C. 2020. Deep-Burial Dissolution in an Oligocene-Miocene Giant Carbonate Reservoir (Perla Limestone). *Gulf of Venezuela Basin: Implications on Microporosity Development. Marine and Petroleum Geology* **113**: 104144. https://doi.org/10.1016/j.marpetgeo.2019.104144.

Wang, B. 2016. *A Comparative Study of Tight Sandstone Reservoir*. MS Thesis, Chengdu University of Technology, Chengdu, China.

Wang, Y., Liu, L., Li, S. et al. 2017. The Forming Mechanism and Process of Tight Oil Sand Reservoirs: A Case Study of Chang 8 Oil Layers of the Upper Triassic Yanchang Formation in the Western Jiyuan Area of the Ordos Basin, China. *J Pet Sci Eng* **158**: 29–46. https://doi.org/10.1016/j.petrol.2017.08.026.

Weibel, R., Olivarius, M., Jakobsen, F. C. et al. 2019. Thermogenetic Degradation of Early Zeolite Cement: An Important Process for Generating Anomalously High Porosity and Permeability in Deeply Buried Sandstone Reservoirs? *Mar Pet Geol* **103**: 620–645. https://doi.org/10.1016/j.marpetgeo.2019.02.006.

Worden, R. H., Bukar, M., and Shell, P. 2018. The Effect of Oil Emplacement on Quartz Cementation in a Deeply Buried Sandstone Reservoir. *Bulletin* **102** (01): 49–75. https://doi.org/10.1306/02071716001.

Xi, K., Cao, Y., Liu, K. et al. 2019. Diagenesis of Tight Sandstone Reservoirs in the Upper Triassic Yanchang Formation, Southwestern Ordos Basin, China. *Mar Pet Geol* **99**: 548–562. https://doi.org/10.1016/j.marpetgeo.2018.10.031.

Xi, K. L., Cao, Y. C., Jahren, J. et al. 2015. Diagenesis and Reservoir Quality of the Lower Cretaceous Quantou Formation Tight Sandstones in the Southern Songliao Basin, China. *Sediment Geol* **330**: 90–107. https://doi.org/10.1016/j.sedgeo.2015.10.007.

Xi, S. L., Li, W. H., and Li, R. X. 2008. Hydrocarbon Generation and Reservoir Formation: A Case from Chang 7 Source Rock in Majiatan Area, West Margin of Ordos Basin (in Chinese). *Pet Explor Dev* **35** (6): 657–663.

Xu, Z., Liu, L., Wang, T. et al. 2017. Characteristics and Controlling Factors of Lacustrine Tight Oil Reservoirs of the Triassic Yanchang Formation Chang 7 in the Ordos Basin, China. *Mar Pet Geol* **82**: 265–296. https://doi.org/10.1016/j.marpetgeo.2017.02.012.

Yan, J., He, X., Zhang, S. et al. 2020. Sensitive Parameters of NMR T2 Spectrum and Their Application to Pore Structure Characterization and Evaluation in Logging Profile: A Case Study from Chang 7 in the Yanchang Formation, Heshui Area, Ordos Basin, NW China. *Mar Pet Geol* **111**: 230–239. https://doi.org/10.1016/j.marpetgeo.2019.08.025.

Yang, B., Qu, H., Shi, J. et al. 2021. The Lithological Features of Sublacustrine Fans and Significance to Hydrocarbon Exploration: A Case Study of the Chang 7 Interval of the Yanchang Formation, Southeastern Ordos Basin, North China. *Geofluids* **2021**: 1–22. https://doi.org/10.1155/2021/5583191.

Yang, R. C., Van Loon, A. J. T., Jin, X. H. et al. 2019. From Divergent to Convergent Plates: Resulting Facies Shifts along the Southern and Western Margins of the Sino-Korean Plate during the Ordovician. *J Geodyn* **129**: 149–161. https://doi.org/10.1016/j.jog.2018.02.001.

Yang, Y. T., Li, W., and Ma, L. 2005. Tectonic and Stratigraphic Controls of Hydrocarbon Systems in the Ordos Basin: A Multicycle Cratonic Basin in Central China. *Bulletin* **89** (2): 255–269. https://doi.org/10.1306/10070404027.

Yuan, J., Huang, C., Zhao, F. et al. 2015. Carbon and Oxygen Isotopic Compositions, and Palaeoenvironmental Significance of Saline Lacustrine Dolomite from the Qaidam Basin, Western China. *J Pet Sci Eng* **135**: 596–607. https://doi.org/10.1016/j.petrol.2015.10.024.

Yu, Q., Ren, Z., Li, R. et al. 2017. Paleogeotemperature and Maturity Evolutionary History of the Source Rocks in the Ordos Basin. *Geological Journal* **52** (3): 97–118. https://doi.org/10.1002/gj.3069.

Zhang, F., Jiao, Y., Wu, L. et al. 2019. Enhancement of Organic Matter Maturation Because of Radiogenic Heat from Uranium: A Case Study from the Ordos Basin in China. *Bulletin* **103** (1): 157–176. https://doi.org/10.1306/06071817107.

Zhang, Y., Hu, C., Wang, M. et al. 2018. A Quantitative Sedimentary Model for the Modern Lacustrine Beach Bar (Qinghai Lake, Northwest China). *J Paleolimnol* **59** (2): 279–296. https://doi.org/10.1007/s10933-016-9930-2.

Zhang, Y., Hu, C., Wang, X. et al. 2017. An Improved Method of Laser Particle Size Analysis and Its Applications in Identification of Lacustrine Tempestite and Beach Bar: An Example from the Dongying Depression. *J Earth Sci* **28** (6): 1145–1152. https://doi.org/10.1007/s12583-016-0930-1.

Zhao, J., Liu, C., Huang, L. et al. 2020. Paleogeography Reconstruction of A Multi-Stage Modified Intra-Cratonic Basin—A Case Study from the Jurassic Ordos Basin, Western North China Craton. *J Asian Earth Sci* **190**: 104191. https://doi.org/10.1016/j.jseaes.2019.104191.

Zheng, Q., Liu, X., You, J. et al. 2019. Discovery and Prediction of High Natural Gamma Sandstones in Chang 73 Submember of Triassic Yanchang Formation in Ordos Basin, China. *J. Cent. South Univ* **26** (7): 1840–1855. https://doi.org/10.1007/s11771-019-4138-z.

Zhou, X. W., Jiang, Z. X., Quaye, J. A. et al. 2019. Ichnology and Sedimentology of the Trace Fossil-Bearing Fluvial Red Beds from the Lowermost Member of the Paleocene Funing Formation in the Jinhu Depression, Subei Basin, East China. *Mar Pet Geol* **99**: 393–415. https://doi.org/10.1016/j.marpetgeo.2018.10.032.

Zou, C. N., Zhu, R. K., Chen, Z. Q. et al. 2019. Organic-Matter-Rich Shales of China. *Earth-Science Reviews* **189**: 51–78. https://doi.org/10.1016/j.earscirev.2018.12.002.

Zou, C. N., Zhu, R., Liu, K. et al. 2012. Tight Gas Sandstone Reservoirs in China: Characteristics and Recognition Criteria. *J Pet Sci Eng* **88–89**: 82–91. https://doi.org/10.1016/j.petrol.2012.02.001.

Zvirtes, G., Philipp, R. P., Hurst, A. et al. 2020. Petrofacies of Eocene Sand Injectites of the Tumey Giant Injection Complex, California (USA). *Sediment Geol* **400**: 105617. https://doi.org/10.1016/j.sedgeo.2020.105617.